Acta Geotechnica
https://doi.org/10.1007/s11440-022-01658-7

RESEARCH PAPER

# A micro-investigation of unsaturated sand in mini-triaxial compression based on micro-CT image analysis

Ji-Peng Wang[1] · Ji-Yuan Luan[1] · Xu-Guang Gao[1] · Tai-Heng Liu[1] · Edward Andò[2,5] · Bertrand François[3,4]

Received: 30 September 2021 / Accepted: 5 July 2022


**Abstract**
The mechanical behaviours of unsaturated soils are highly related to the water content and pore water and air distributions. Under the context of climate change, geo-disasters related to soil moisture change attract more and more research attentions. Due to the heterogeneity of soil textures and the complicated morphology of liquid phases, it is crucial to understand the microstructural features of unsaturated soils. This work presents a study based on a miniaturized suction controlled triaxial device which is suitable for micro-CT image analysis. A fine sand is sheared in this device under different suction levels while CT scans are taken at different strain stages. After image 3D reconstruction, image trinarization, label analysis, contact detection and other customized image analysis and calculations, the micro-mechanisms of unsaturated granular soils upon triaxial shearing are investigated. It is observed that the inter-particle contact coordination number is reduced after shearing due to the dilation behaviour and the sample with the highest capillary strength has the highest coordination number. Although there is an initial fabric anisotropy due to gravity and sample compaction, triaxial loading will further enlarge the fabric anisotropy of the solid phase and the solid fabric anisotropy is also associated with shear strength. With the development of shear band, water drains out and the quantity of small-volume liquid clusters in the liquid bridge increases. This shifts the distributions of inter-facial areas. The effective stress tensor is interpreted microscopically based on small RVEs. Based on the CT image analysis, the suction-induced stress component is not an isotropic term and the anisotropy of the water phase is increased with triaxial deformation as well as decrease in degree of saturation when there are more isolated water bridges formed around solid contacts.

**Keywords** Fabric anisotropy · Micro-scale · Triaxial test · Unsaturated soil · Water distribution · X-ray CT

## 1 Introduction

Unsaturated soil, as a mixture of solid, liquid and gas phases, is the most common state of soil on the earth surface as the surface soil is normally above the groundwater level. The mechanical behaviours of unsaturated soils are highly related to soil moisture and pore water distributions. Climate change is believed to be a exceedingly vital challenge to all human beings. Extreme weather events, such as draughts and excessive rainfalls causing soil water content fluctuating, may furtherly lead to unfavourable soil property changes including soil deformation (both shrinkage and swelling) and strength loss which are the main causes to geo-disasters of slope failure, embankment settlement, etc. [16, 36]. Therefore, unsaturated soil mechanics, as a branch of classic soil mechanics, has developed rapidly in the past two decades [1, 12, 25, 26].

✉ Ji-Peng Wang
Ji-Peng.Wang@sdu.edu.cn

1 School of Civil Engineering, Shandong University, Jingshi Road 17922, Jinan 250061, China

2 Laboratoire 3SR, Université Grenoble Alpes, F-38000 Grenoble, France

3 Department of Urban and Environmental Engineering, University of Liège, Allée de la Découverte 9, Quartier Polytech 1, 4000 Liège, Belgium

4 Building Architecture and Town Planning Department (BATir), Université Libre de Bruxelles, Avenue F.D. Roosevelt 50, CP 194/2, 1050 Brussels, Belgium

5 Present Address: EPFL Center for Imaging, École Polytechnique Fédérale de Lausanne (EPFL), 1015 Lausanne, Switzerland

Published online: 02 September 2022

However, due to the heterogeneity of soil textures and the complex morphology of liquid–air interfaces [33], an accurate description/prediction of the stress–strain behaviour of unsaturated soil from its global stress states is still a challenging task [12, 25]. This leads to arguments in basic theories of unsaturated soils and therefore limited the engineering applications of the new theories.

Therefore, to understand the hydro-mechanical behaviours of unsaturated soils from soil particle interactions as well as pore-scale liquid–air interactions is crucial for macro-scale theory development and validations. In the past two decades, numerical approaches are employed to study the micro-scale behaviours of partially saturated granular soils, including the discrete element method (DEM) [11, 34, 42–44], level set method [37] and the lattice Boltzmann method (LBM) [30, 31, 46]. However, these numerical methods have different drawbacks to study unsaturated soil behaviours. In DEM, the particles are commonly idealized as spherical particles, and the capillary effect is usually simulated as individual water bridges which limits the applicable water content range. In level set and LBM, hydraulic behaviours and pore water distributions can be numerically simulated but the calculation is normally time consuming and the size of the model is limited to a relative small scale. In addition, none of the numerical methods can replicate the local variations of contact angles and pore structures without experimental evidences.

X-ray CT tomography, which was originally developed as a medical diagnostic tool [8, 17], becomes an increasingly popular experimental approach in the research of geomaterials due to its non-invasive and non-destructive features [6, 20, 38, 45]. It has been used to study the local porosity and local pore structures of granular soils [7, 24, 35], individual particle shape and motions [5], as well as strain localizations [2, 3, 10, 13, 14, 40]. Due to the limitation of image resolution, granular materials such as sand and glass beads are more suitable materials for CT scans. As for the study of unsaturated soils, the CT technique has also attracted more attention in the recent years, but the quantity of the work is still limited. Different researchers have investigated the mechanical behaviours of unsaturated granular soils (mainly the morphology of liquid phase and the deformation characteristics of the solid structure) [4, 15, 18, 27–29], the hydraulic properties of unsaturated granular soils (such as water retention behaviours) [21, 23, 32], and recently scholars are trying to link the microscopic characteristics to the macroscopic responses combining with X-ray CT scanning technique [22]. However, the coupled hydro-mechanical behaviours of unsaturated granular soils still need more research efforts from the microscopic point of view.

Suction controlled triaxial test is a fundamental experiment to understand the hydro-mechanical behaviours of unsaturated soils. However, the commercially supplied devices are not suitable to be used in combination with X-ray CT directly due to its metal parts. The standard sizes of the device and the soil sample also limit the CT image resolution as in a cone X-ray beam the magnification factor is inversely proportional to the size of the scanned object. In this study, we used a customized mini-triaxial device made of transparent Plexiglas materials and sizes of the device and the installed soil sample are also miniaturized [41]. The device is employed to study the stress–strain behaviours of an unsaturated granular soil under different constant suction levels. CT scans are taken at different axial strains to study the microscopic behaviours upon triaxial loadings. After image trinarization, labelled analysis of solid and water phases, interfacial areas analysis and inter-particle contact detections, the macroscopic behaviours will be explained from the microscopic point of view including the evolution of the water cluster distributions, the global and local interfacial areas, distribution of coordination numbers. Moreover, the loading-induced anisotropies in the solid structure and the water phase are also recorded and analysed, which will help the understanding of the controversial concept of effective stress of unsaturated soil.

## 2 Experimental set-up

### 2.1 Properties of the tested sand

A commercially supplied Mol sand is used to prepare the experimental sample. The filled and compacted Mol sand is a fine sand with grain diameter ranging from 0.06 to 0.6 mm. It has a coefficient of uniformity $C_u$ of 1.44 and a median grain size $D_{50}$ of 0.265 mm making it poorly graded sand. The grain size distribution curve of the tested sand is shown in Fig. 1a. The water retention curve of the Mol sand is depicted in Fig. 1b which was measured from a drainage process by using a hanging water column method.

### 2.2 The miniaturized testing device

The sketch of the developed miniaturized triaxial test device is presented in Fig. 2a. Main part of mini-triaxial device is made of plexiglas material which permit X-ray beams effectively penetrate the mini-device and the soil sample without significant energy loss. Meanwhile, the experimental device is based on the same principle of conventional triaxial test devices but with a miniaturized size to obtain a higher resolution in the X-ray CT system. The soil sample is in cylindrical shape with 10 mm in

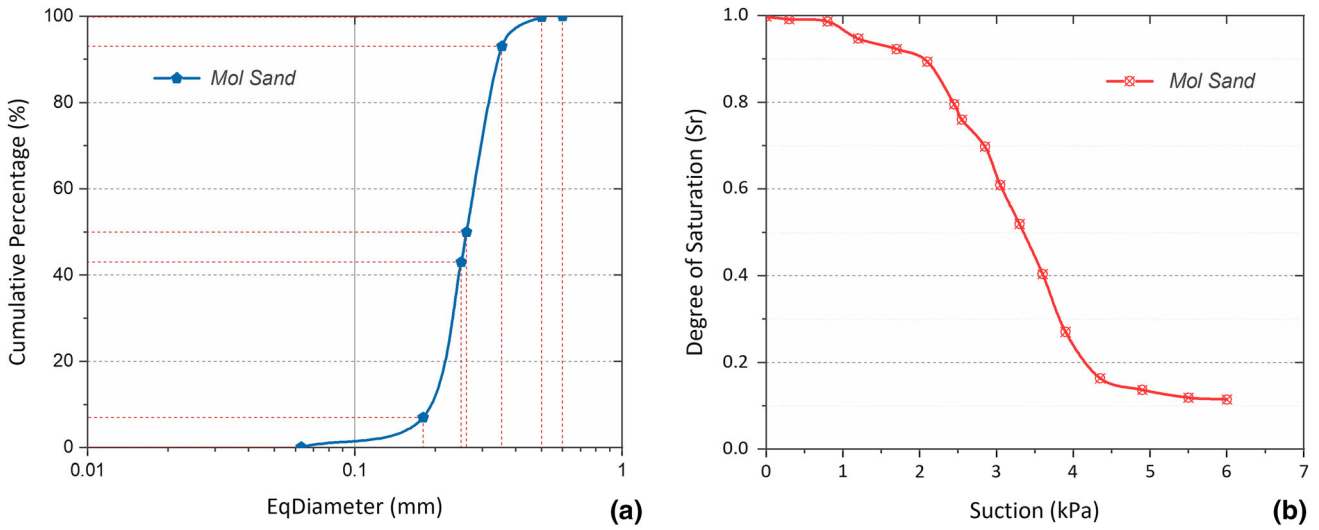


**Fig. 1** **a** Grain size distribution of the tested sand; **b** water retention curve of the tested sand

diameter and 20 mm in length. The outer diameter of the plexiglas pressure chamber is 60 mm. Utilizing the micro-stepper motor to precisely control the axial strain of sample, and a submersible force sensor is employed and inserted into the axial piston in the confining chamber to avoid the friction effect between piston and the chamber orifice in force measurement.

The triaxial cell is fixed on a rotational table between the X-ray beam source and the detector with data acquisition unit connected to conduct X-ray CT scans during triaxial tests at various strain stages. The specific setting configuration is displayed in Fig. 2b. As the main deformation of the samples in triaxial test occurred in the middle part, a 12-mm-long region of interest is taken in that part as the studied object throughout this paper.

### 2.3 Experimental procedures and parameters

The fine sand sample is prepared and compacted in a cylindrical mould with a rubber membrane sticked on its inner wall. After sand filling and compaction, the top cap is assembled on the top of the sample and then sealed with an O ring. Before removing the cylindrical mould, a vacuum condition is applied to the sample by using a vacuum air pump through the bottom channel (top channel is closed). This is to keep the sample vertically during the device assembling. After assembling different parts of the mini-triaxial device, water is filled in the triaxial cell and 16 kPa cell pressure is maintained by a pressure controller. The bottom channel is connected with a water reservoir, and after completing the above procedures, the valves are opened to allow water inflow to saturate the soil sample. By keeping the sample connecting to the atmospheres air through the top channel, the water reservoir is lowered to a certain level to apply suctions (four tests with 2, 2.5, 3 and 4 kPa suction values are applied in this study). It takes approximate 20 min to reach the equilibrium state after applying suction. Evaporation and room humidity have little effect on the test as there is no obvious change of water level during the test.

X-ray CT scans are performed at different strain stages (0, $\approx$ 2, $\approx$ 5, $\approx$ 10 and $\approx$ 15%) when the axial loading is ceased by pausing the micro-step motor motion. For keeping fully drained conditions of sample, the loading rate is set as $2.5 \times 10^{-4}$ s$^{-1}$. Generally, CT slices with high image resolution could be regarded as good CT scanning results, which requires either a small focused area or a large number of scanned positions (therefore longer scanning time). The in situ miniaturized trixial shearing CT scanning tests were conducted by using the micro-focus X-ray CT in Laboratoire 3SR, Grenoble, and the adjusted same CT scanning parameters were used for each scan. The applied voltage is 100 kV at 10 W power. A region of interest (ROI) in the middle part of the sample with 1.2 cm long and 1 cm in diameter is taken to perform the X-ray CT scans (2 h per scan). The obtained image resolution is 9 µm/pixel, which is close to the best resolution of this experimental system (the micro-CT scanner combining with mini-triaxial device).

## 3 Image analysis methodologies

### 3.1 Image trinarization

The series of raw X-ray projections obtained from the micro-CT scans are then reconstructed into greyscale CT slices before image processing. The three-dimensional

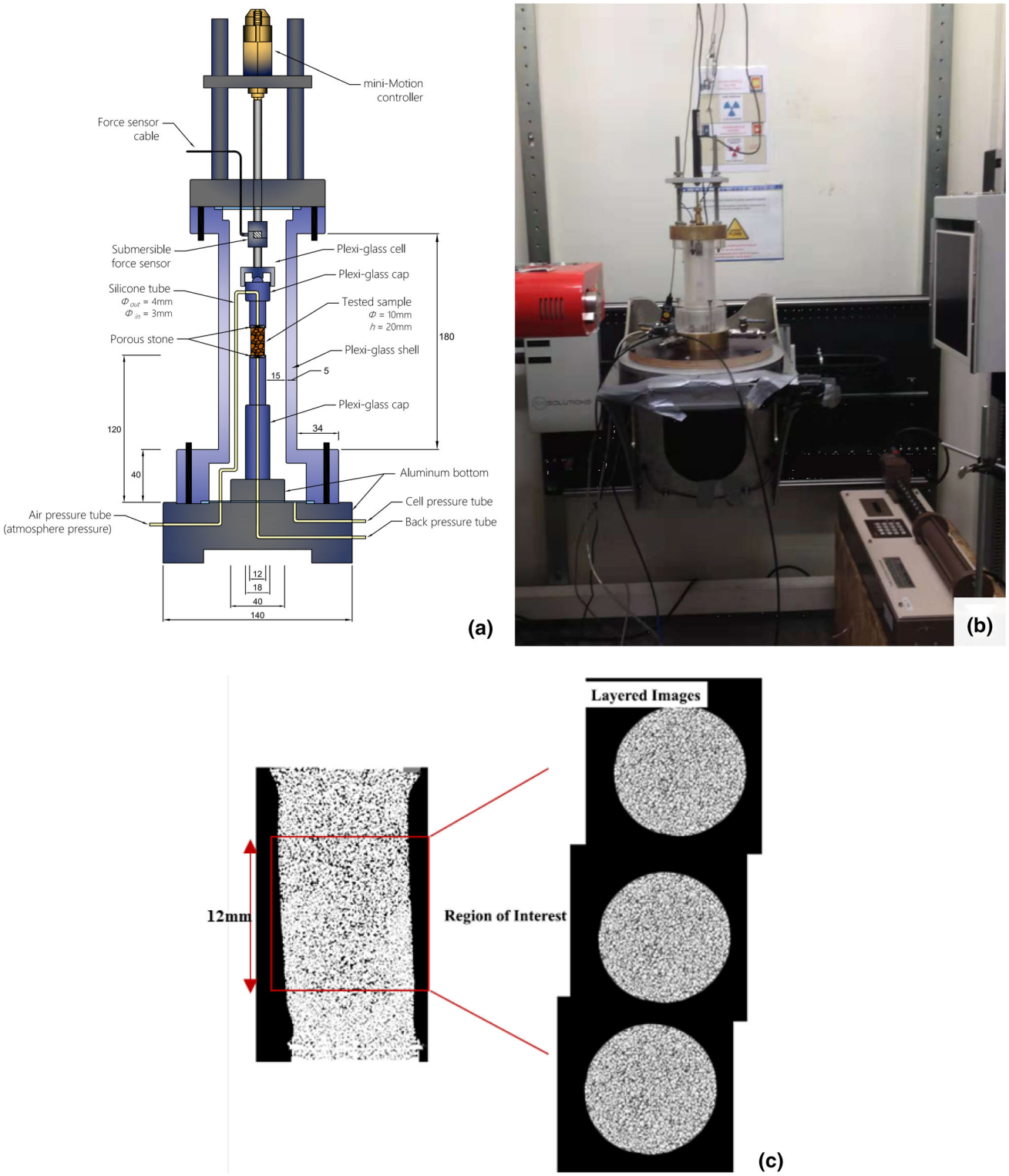


**Fig. 2** **a** The miniaturized triaxial device; **b** the X-ray scan set up; **c** 10 mm length ROI studied in this paper

sample is represented in the form of a two-dimensional (2D) slices stack. Each voxel (pixel in 2D slices) has a particular grey level, which is associated with its representing phase (air, water or solid).

This is because objects with different densities have different attenuation effects on the X-ray beams penetrating them, resulting the greyscale CT images which show different greyscale levels for each phase representing

different substances. Figure 3 shows the grey-level distributions of the scanned soil sample with different axial strain at different suctions states, and the three peaks are air, water and soil grain, respectively. The peak represented by solid phase is comparatively steady for different suction values; nevertheless, there is an evident trend that the peak is represented by air phase gradually lifting with the increase in suction and the liquid-phase peak oppositely decreasing at the same time. The process of drainage and air entrance could be directly reflected by this fluctuation of the two corresponding phases. The three phases are generally in normal distributions, but there are overlaps due to the noise generating in CT scanning process and partial volume effects (PVE) existing at the boundary between different phases, which could directly affect the accuracy of result about segmentation.

After X-ray projections reconstruction, all the obtained raw greyscale CT slices were registered to a same coordination system and the image dimension of the entire field of view is 1500 × 1500 × 1350 (x*y*z) voxels. Then, the open-source software ImageJ is employed to pre-process the raw CT images with the same operation steps and parameters to ensure that the grayscale distribution of each group of adjusted raw images is in a close grey-level range, and the corresponding grayscale range of the three-phase peaks in each group CT images remains highly consistent. The commercial software Avizo-2019 is used to complete the image trinarization (Fig. 4 shows the process of trinarization, and Fig. 5 displays the trinarized result of the sample at s = 2 kPa and ε ≈ 2% as an example) and series of subsequent analysis. Initially, a non-local means filter is applied for noise reduction with preserving edge between two different phases before image trinarization and the subsequent image information analysis. The filtered greyscale images with smoothed phase interior and preserved

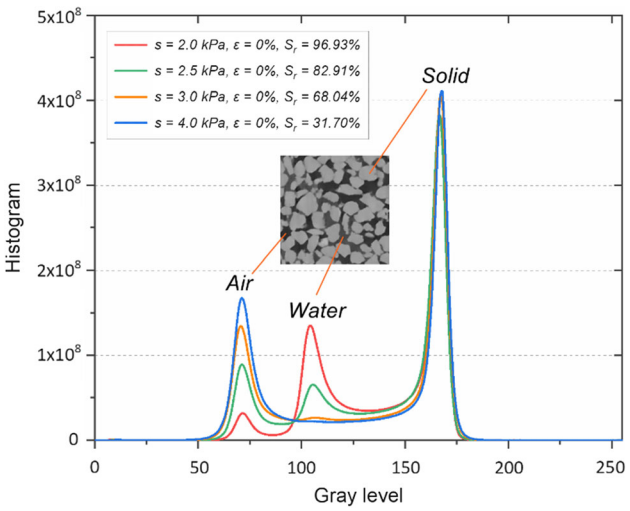


**Fig. 3** Grey-level distribution histogram

edge are segmented into three phases (soil grains, water and air) to generate 3D trinarized images by utilizing a seeded watershed algorithm, in which seeds of the three phases are generated by setting the partial threshold based on selecting the grey value of the range near the corresponding peak value of the three phases in grey-level distribution histogram. The greyscale gradient images are used to define the boundary between any two neighbouring phases, as constraints for the three-phases segmentation. The phase classification error caused by PVE can be effectively avoided by this segmentation method, which improves the accuracy of subsequent images analysis.

Evolutions of void ratio and degree of saturation of the sample during the triaxial compression test can be measured by the trinarized 3D CT images. The trinarized 3D images provide an alternative and mutually independent way for measuring the volumes of the three phases within the specimen, those volumetric parameters (i.e. $V_t$—total volume, $V_v$—pore volume, $V_s$—solid-phase volume, $V_w$—liquid-phase volume, $V_a$—air-phase volume) can be obtained directly by counting the number of voxels of each phase. Meanwhile, summing the relevant number of voxels in each phase can calculate the degree of saturation $S_r = V_w/V_v$ and the void ratio $e = V_v/V_s$.

## 3.2 Labelled analysis of sand particles and water clusters

The 3D trinarized images are used to extract the solid phase (soil grains) and the liquid phase (water) for labelled analysis. For solid phase, it is segmented from the trinarized images and converted it to a binarization form (including only solid grains and voids). The soil grains with adhesion zone (inter-particle contacts) in binary image of the extracted solid phase are then 'separated' into isolated particles by Avizo. This command module is a high-level combination of watershed, distance transform and numerical reconstruction algorithms, which could be used to detect and remove the adhesion zone (inter-particle contacts) between the particles. Later, soil particles are labelled and each particle is allocated a unique identification (ID) and a colour. More information about each grain (i.e. the ID number of particles, the centre of mass, 3D volume, 3D area, equivalent diameter, etc.) are obtained by using the tool 'Label Analysis'. The equivalent diameter is the diameter of a sphere which has the same volume of the concerned particle. Figure 6a details solid-phase processing steps in 2D for simplicity, although the real process is 3D.

According to the equivalent diameter information of soil particles obtained from CT image analysis, the particle size distribution curve is drawn in Fig. 7a. The shape and trend between the curves representing soil particle size sieve

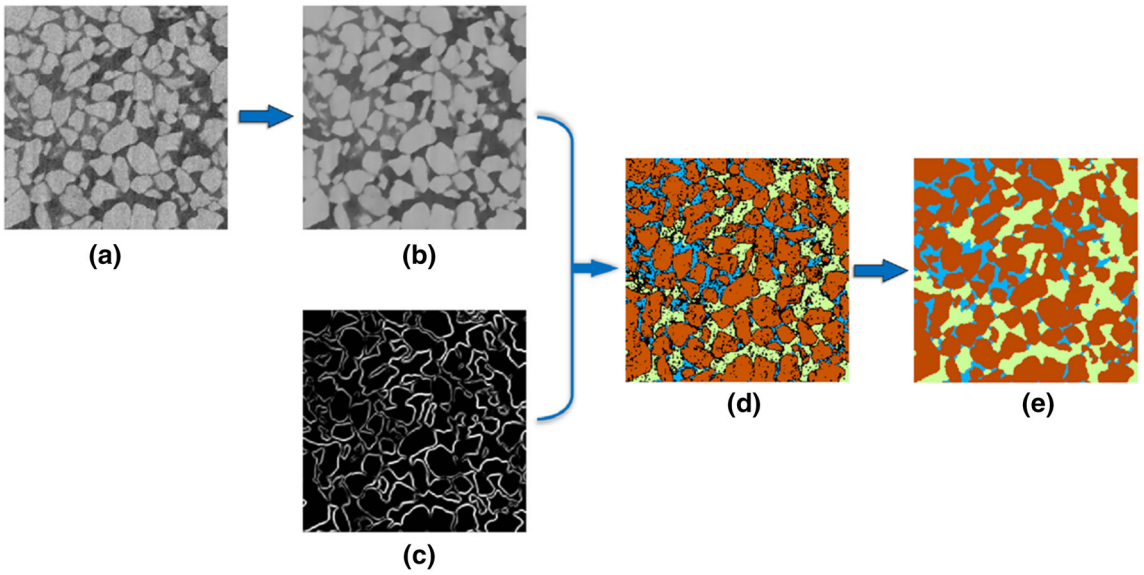


**Fig. 4** Process of image trinarization of the three-phased material: **a** raw CT image; **b** filtered CT image; **c** greyscale gradient image; **d** partial thresholding image; **e** trinarized image

analysis result and CT image analysis results are both quite close, which verifies the methods of solid phase segmentation and soil grain separation. Nevertheless, there is an inevitable difference existing in those groups that the equivalent particle diameter curves of the CT image analysis group are slightly larger comparing with the sieve analysis curve. During the process of sieving soil grains, errors may exist when classifying soil grains with long and narrow shapes (within the roundness range of standard Mol sand), because slender particles may go through the screen mesh and drop into next level sieve. However, the approach to obtain the equivalent diameter of each grain base on the labelled CT images of soil particles is by converting the separated soil grain to the equivalent volume sphere, further utilizing the diameter of equivalent volume sphere as the equivalent diameter of corresponding particles. Meanwhile, a small amount of soil grains with tightly large inter-particle contact area existing in pairs have the possibility of being misclassified. Those above mentioned conditions reflect the reason why the particle size distribution curves measured by CT image analysis are slightly larger than the sieve analysis curve.

The image processing approach for labelling water clusters is similar to labelling solid particles but without the comprehensive watershed algorithm module approach. Firstly, the liquid phase is extracted from the whole 3D volume of trinarized images. Then, water clusters are labelled by using 'Label Analysis' command, and labelling process can be summarized as giving each individual water cluster an identification (Id). This Id is represented in the images by different colours (i.e. each colour represents a specific water cluster). Figure 6b illustrates liquid-phase processing steps in 2D.

### 3.3 Detection of inter-particle contacts

According to the result of the soil particle segmentation, a marker-based watershed algorithm is performed on the filtered greyscale images and binary images, which could obtain the watershed lines of solid phase and further extract the inter-particle contacts. Additionally, the binary images of solid phase are filtered by applying the opening operation (including erode and dilate on phase boundaries) to clear the isolated small volumetric noisy voxel points generated in the hysteresis thresholding process. The extracted contacts are efficiently obtained by performing the arithmetic operation between the binary images of the solid phase and the binary images of the watershed lines.

There are two situations of the position between the solid phase and the watershed lines in the superimposed images, overlapping and separation. When a watershed line pass through the overlapping zone between any two touching particles in the binary images, it could be regarded as the location of the contact of the two touching particles being detected by watershed lines successfully. Nevertheless, if any two neighbouring particles are isolated, the watershed lines pass through the inter-particle voids. The detection and extraction process of the inter-particle contacts is illustrated in Fig. 8.

Then the extracted contact areas (in voxels) are analysed by the 'Label Analysis' command just as the analysis of individual particles. Each extracted inter-particle contact is labelled and the morphology information of the contact

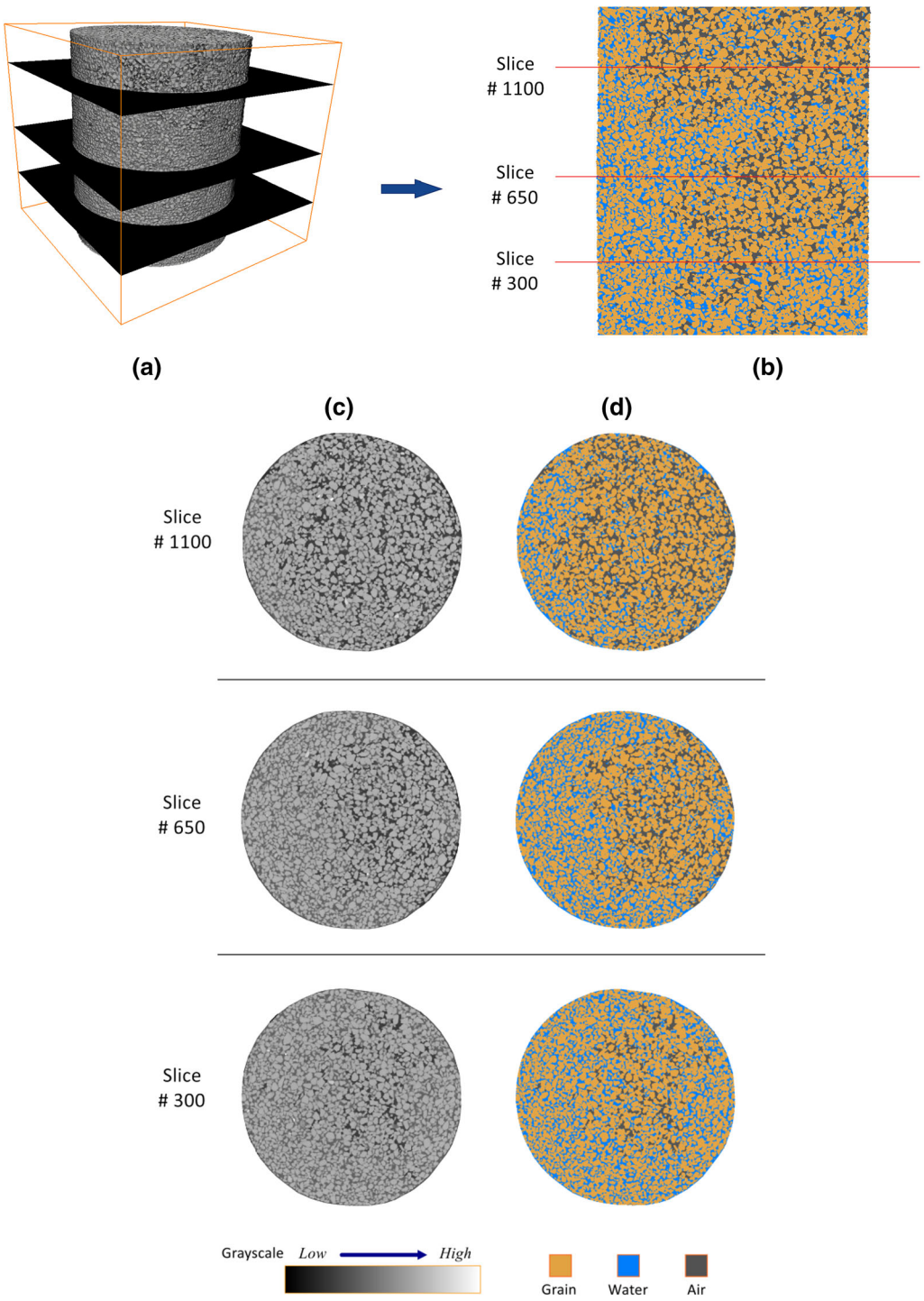


**Fig. 5** Selected trinarized image for the triaxial sample at s = 2.0 kPa, $\varepsilon \approx 2\%$, **a** reconstructed 3D greyscale model and the selected locations; **b** trinarized vertical central slice; **c** greyscale horizontal slices; **d** trinarized horizontal slices

(i.e. the ID number, the centre of mass, 3D volume, the 3D thickness of the contact, the vector of the 3D thickness, etc.) are obtained. The 3D thickness is determined as the largest segment that touches the object by its end points and lying in a plane orthogonal to both the maximum 3D Feret diameter (length 3D) and the breadth 3D diameter.

Meanwhile, the orientations of the extracted inter-particle contacts are determined by the angle $\varphi$ between the normal vector and the $z$-axis, the 3D thickness obtained by applying 'Label Analysis' command conforms to the definition of the normal vector of the contact area, and therefore, the coordinate information of the 3D thickness is

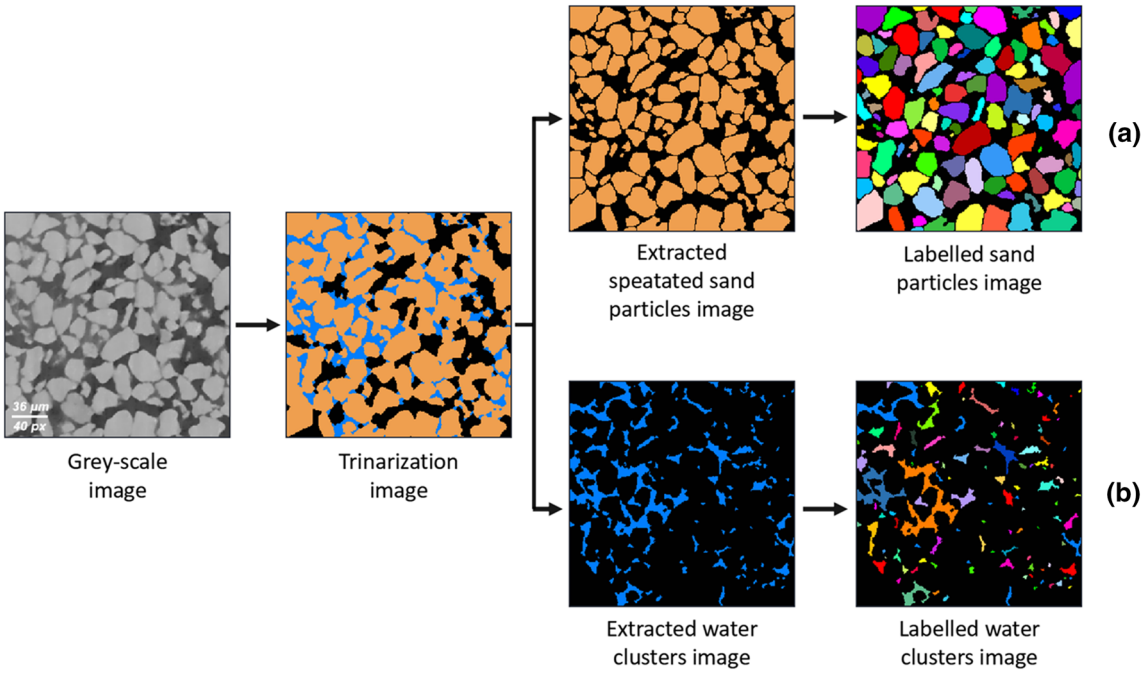


**Fig. 6** **a** Labelled sand particles; **b** labelled water clusters

capable of computing the normal vector of the contact. And the approach of determining the extracted inter-particle contact orientation is illustrated in Fig. 9.

### 3.4 Determination of interfacial area

The representative volume element (RVE) method is utilized to quantify the local information by meshing samples into cubic RVEs, and choosing the 110 pixels ($\approx 1$ mm) as the RVE length to mesh the sample into cubic elements. A full description of the image processing about determination of the RVE size can be found in a previous work by Wang et al. [41].

The interfacial areas of the segmented trinary images can be calculated by following the algorithm of Dalla et al. [9]. In MATLAB, the isosurface function is employed to convert the surface of a phase originally formed by cubic voxels into a smoother surface. The surface areas of the solid phase, the wetting phase (water) and the non-wetting phase (air) are firstly calculated from the trinarized images, and then the specific air–water interfacial area $a_{aw}$ can be calculated as Eq. (1):

$$a_{aw} = \frac{1}{2}(a_n - a_s + a_w) \tag{1}$$

and the specific solid–water interface area $a_{sw}$ can be calculated as Eq. (2):

$$a_{sw} = \frac{1}{2}(a_s - a_n + a_w) \tag{2}$$

where $a_n$ is the specific surface area of the non-wetting phase (air), $a_s$ is the specific surface area of the solid phase and $a_w$ is the specific surface area of the wetting phase (water) (specifically see Fig. 10).

### 3.5 Determination of coordination number

The evolution of inter-particle contacts such as coordination number (CN) is a fundamental aspect for characterizing the change in microstructures. The inter-particle contact occurrence is detected by following a similar concept of characterizing pore connectivity. Firstly, the binary images of the solid phase are imported into a pore network modelling (PNM) module with the graphic information of voids and the unseparated soil particles with adhesion areas (inter-particle contacts) being included. Then these unseparated soil particles are regarded as the 'pores' originally defined in the PNM module for analysing the coordination number (CN) of each soil particles. And the inter-particle contact zones are regarded as the 'pore throats' in the PNM module.

It should be noted that the same comprehensive watershed algorithm for separating grains as mentioned above in Sect. 3.2 is also applied in the PNM module to perform soil particles segmentations inside the solid phase. Therefore, the output labelled images of the two operations show high similarity, and the difference of them is whether containing the adhesion zone (the red extracted inter-particle contacts in Fig. 11a) between grains in the output image. Figure 11b and c displays the labelled image results of separated grains

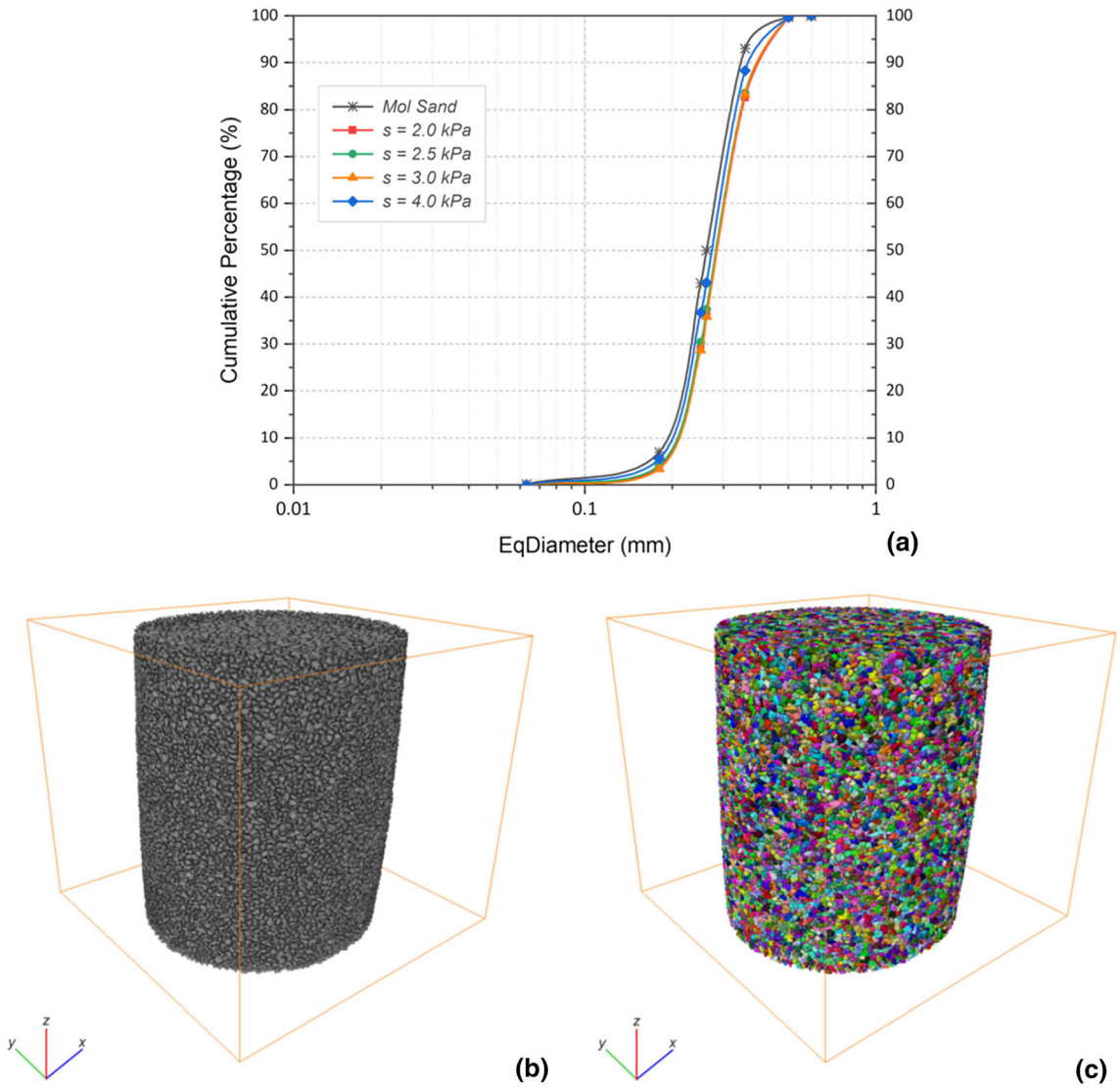


**Fig. 7** **a** Comparison of particle size distribution curves between sieve analysis and CT image analysis; **b** reconstructed 3D soil grains model; **c** labelled 3D reconstruction soil grains model

and segmented solid phase, respectively. Those figures revel the inter-particle contact area is not eliminated, and the adhesion zone between grains is remained during the coordination number analysis in PNM module. Actually, the obtained CN data are defined by counting the number of contacts per particle, and the technical method of PNM module in Avizo software is utilized to achieve statistics about the value of CN.

## 4 Macroscopic and microscopic behaviours

### 4.1 Macroscopic behaviours

Figure 12a depicts the evolution of deviatoric stress of the Mol sand sample during the triaxial compression test under four different suction conditions and a constant confinement of 16 kPa, and the behaviour of a dry sample is also presented as a reference. The soil sample is scanned at five different strain stages (i.e. the axial strains ε is approximately of 0%, ≈ 2%, ≈ 5%, ≈ 10% and ≈ 15%), and the scanning points are marked in Fig. 12a.

The strength for each suction is considered as the maximum deviatoric stress reached by each curve. This strength is maximum (q = 70 kPa) for an intermediate suction level (s = 2.5 kPa) at a deformation of around 10%. Generally, the unsaturated samples have higher material strength. For the specimens subjected to the suction of 4 kPa, the quantity of water stored in the meniscus after water drainage is not strong enough to produce a significant strength enhancement, so the curve represented

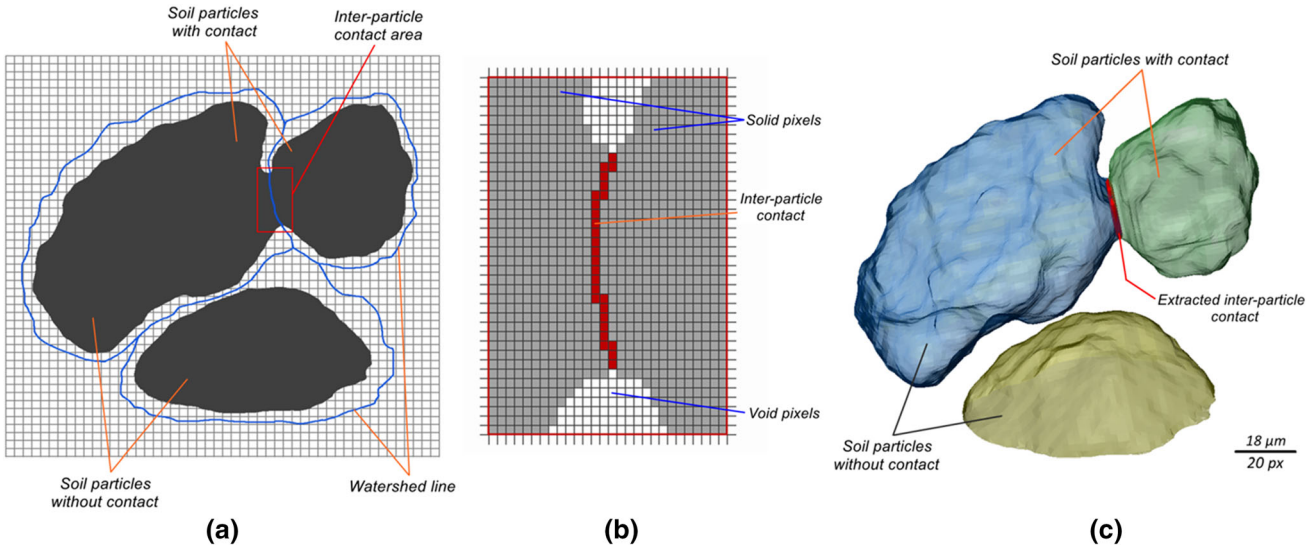


**Fig. 8** Determination of inter-particle contacts, **a** illustration of soil particles with contact; **b** illustration of inter-particle contact area; **c** reconstruction 3D model of soil particles with inter-particle contact after X-ray CT scanning

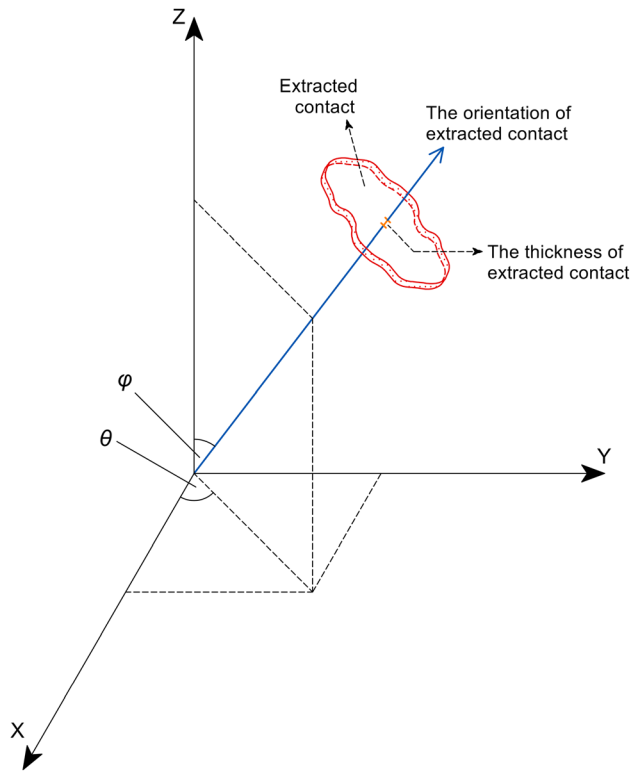


**Fig. 9** Determination of contact orientation

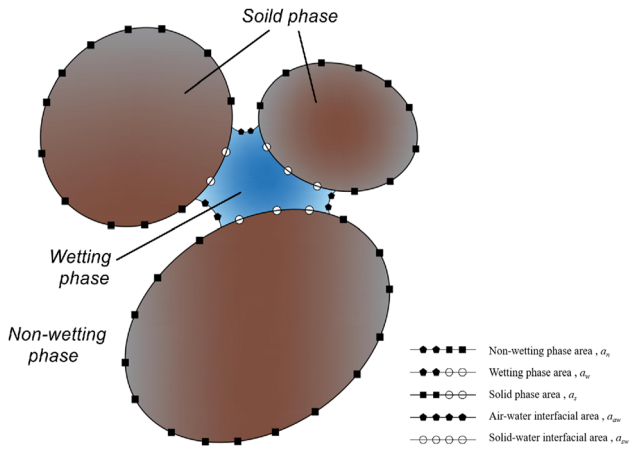


**Fig. 10** Illustration of the phases interfacial area

by s = 4 kPa is quite close to the reference curve of the dry sand.

Then, during triaxial shearing, the evolutions of the void ratio and degree of saturation with axial strain are presented in Fig. 12b and c, respectively. Loading-induced deformation leads to the volume of void increase (due to dilatancy upon shearing) and water desaturation within the sample. Consequently, the samples under different suction controlled conditions all showed an increasing trend in void ratio and a decreasing trend in degree of saturation. It can also be seen that after shearing (axial strain $\varepsilon \approx 10\%$ and 15%) the increase in porosity slows down and stabilizes. The dilatancy is more obvious in the test under a higher suction, as the void ratio increase during the triaxial loading is higher.

In Fig. 12c, with the increase in the applied suction and the growth of the axial strain, the overall trend of degree of saturation is in decreasing. As can be seen from the lower suction value state, the initial and final degrees of saturation values are both higher. This indicates that water inside the sample is drained during the triaxial shearing process, with the total sample volume expanding and the porosity being enlarged, which is directly shown in Fig. 13. It can also be seen that there are more water drains out in samples

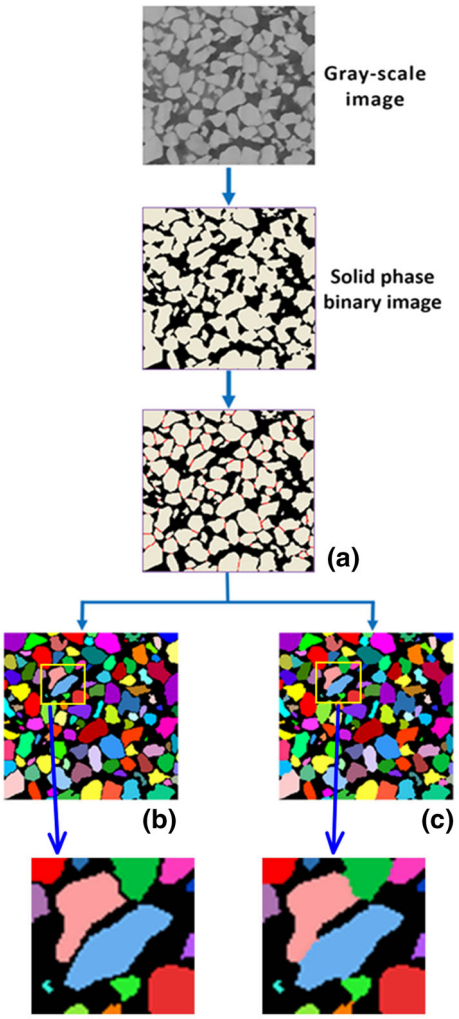


**Fig. 11** The comparison between soil particles separation and solid phase segmentation, **a** solid phase binary image with extracted inter-particle contacts; **b** separated and labelled solid phase image; **c** segmented and labelled solid phase image in the PNM module

with lower suction. And at the final stage, the degree of saturation curves tends to be stable, which is similar to the stabilized trend in the void ratio curves.

## 4.2 Evolution of water clusters

The process of extracting and labelling liquid phase is shown in Sect. 3.2, which is very useful to refer to any water cluster directly by its Id number. Further information of each labelled water cluster (i.e. the ID number of particles, the centre of mass, 3D volume, 3D area, equivalent diameter, etc.) can be obtained based on the labelled water clusters images. The obtained information is used to plot liquid cluster size distribution, which is similar in concept to the particle size distribution. It represents the relation between cluster dimension and the cumulative volume of the clusters. And the evolution of water cluster size

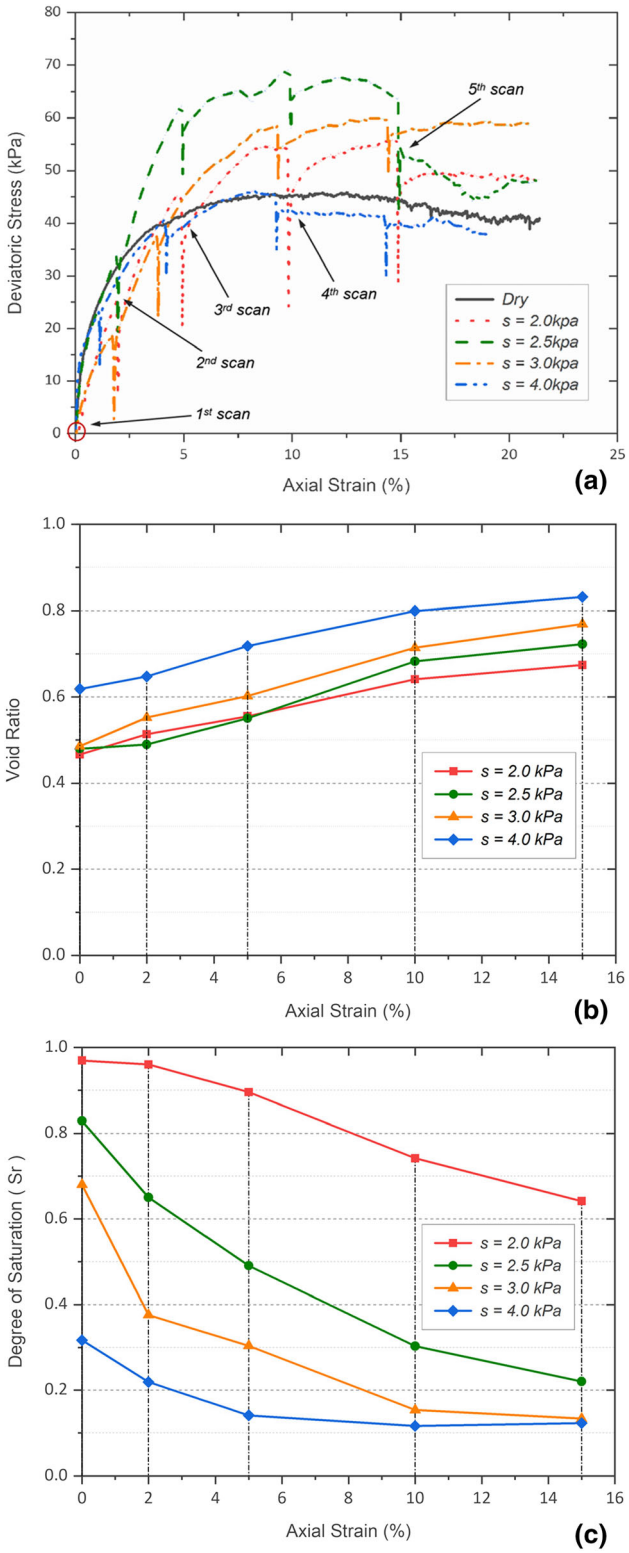


**Fig. 12** **a** Relationship between axial strain and deviatoric stress; **b** relationship between axial strain and void ratio (based on image analysis of the sample); **c** relationship between axial strain and degree of saturation (based on image analysis of the sample)

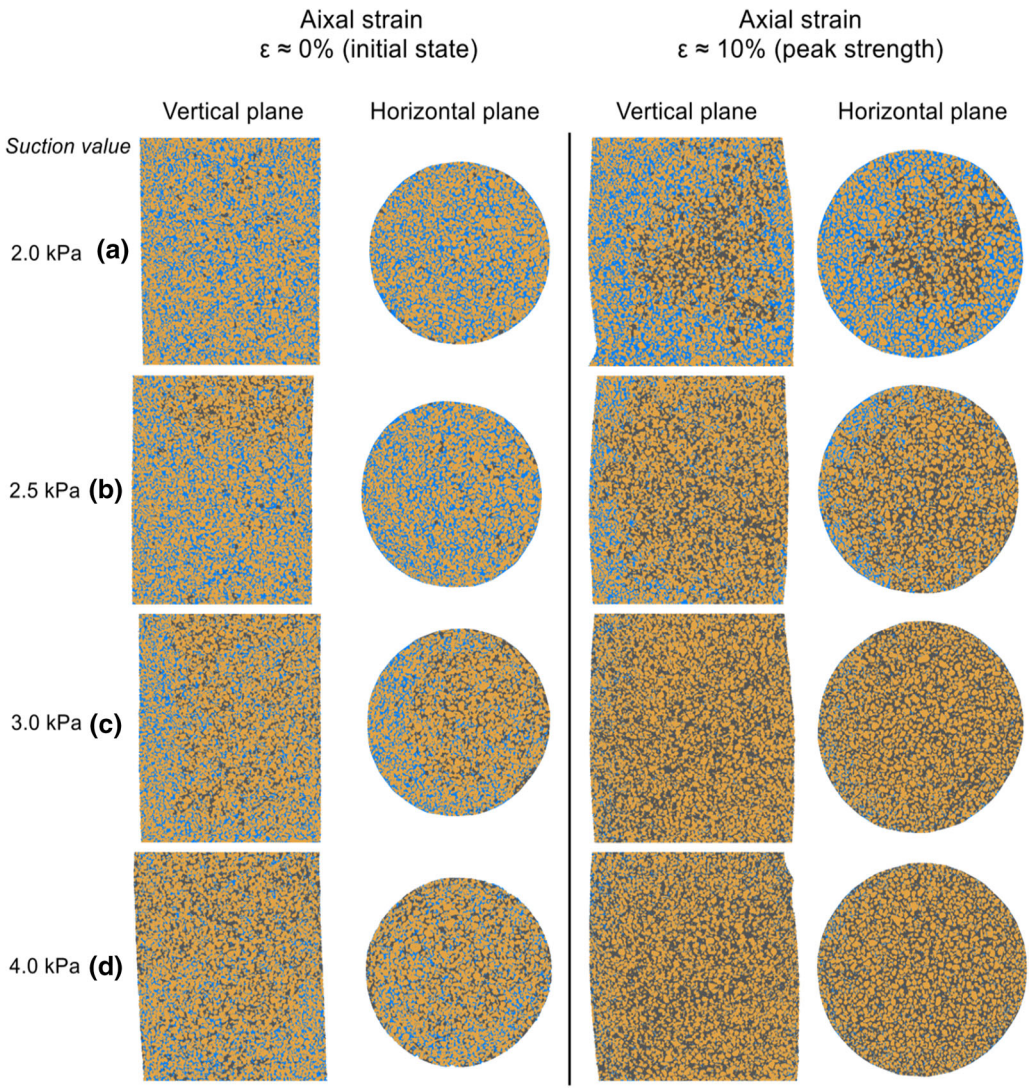


**Fig. 13** Trinarized horizontal cross section at initial and peak strength (ε = 0% and ε ≈ 10%): **a** s = 2.0 kPa; **b** s = 2.5 kPa; **c** s = 3.0 kPa; **d** s = 4.0 kPa

distributions at different strain state during triaxial tests under various constant suction conditions from 2.0 to 4.0 kPa is plotted in Fig. 14. For each water cluster size distribution curve, there is an isolated point located on the upper right corner in these four figures which is not continuous with the main curves indicating there is a large volume liquid cluster.

The test starts from a nearly saturated specimen where the water phase basically presents as one whole large cluster. When different suction is maintained (from s = 2.0 to 4.0 kPa) and the axial strain is continuously applied (from ε = 0 to ε ≈ 15%), the big water cluster divides into smaller clusters and thus the number of clusters increases; meanwhile, the equivalent volume of the largest water cluster inside sample decreases as the controlled suction increases. In Fig. 14, both the uplift of the continuous distribution curves representing the splitting of large water clusters into smaller ones and the decrease in the isolated points representing the largest water clusters are graphically expressed.

Under 2.0 kPa and 2.5 kPa suction conditions, the quantity of small clusters rises with the axial strain increasing, and at the same time the saturation of the sample decreases but strength of the sample grows correspondingly. As the suction is being increased, the proportion of small clusters continues to increase and it reaches a maximum value at s = 3.0 kPa; approximately half of water volume is discontinuous in the form of small water clusters when the specimen is sheared. During the triaxial shearing process, the quantity of small-volume water clusters or water bridges existing in inter-particle zones increases, which results in the uplift of the continuous

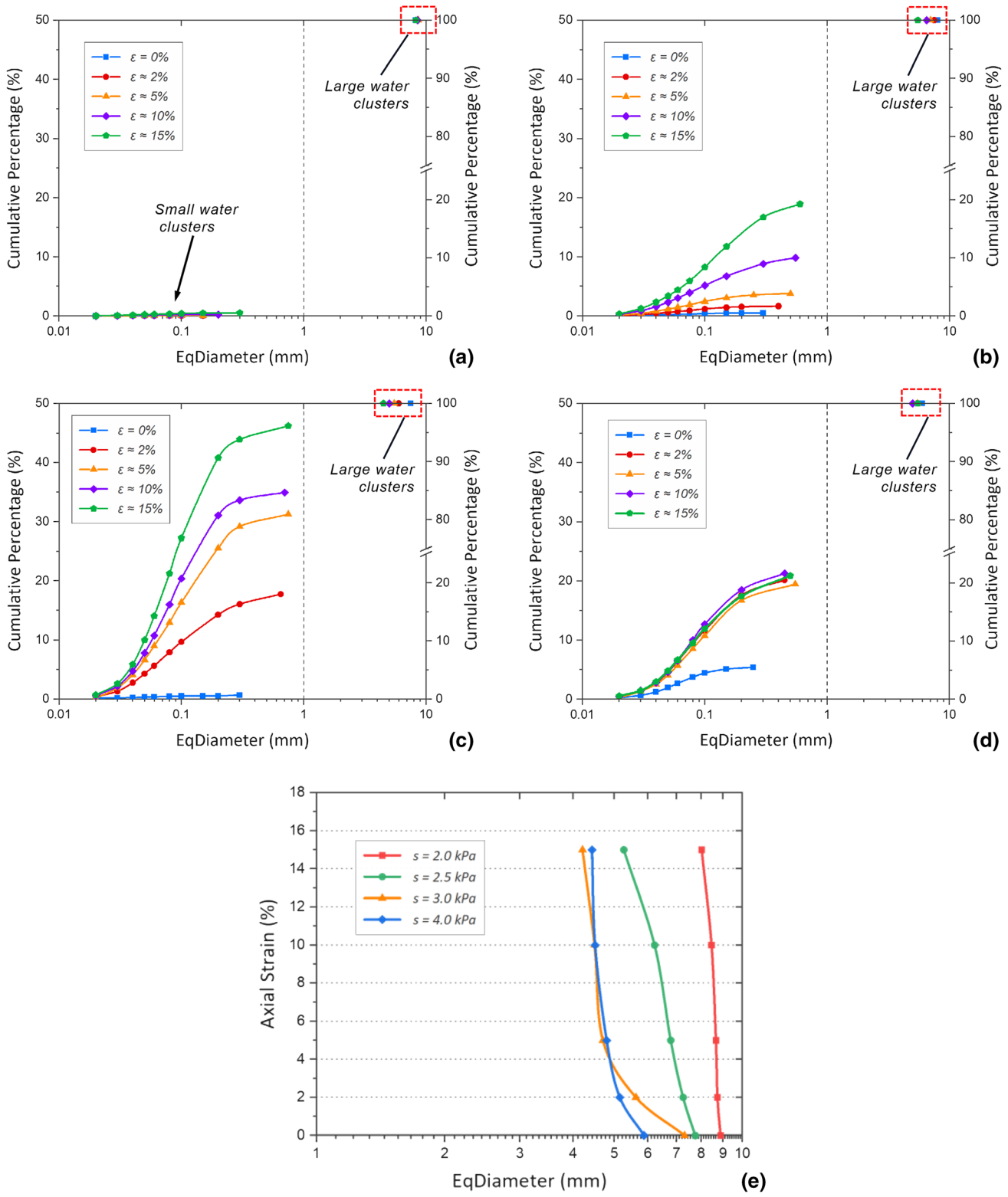


**Fig. 14** Evolution of water cluster size distributions at different suction and strain conditions: **a** s = 2.0 kPa; **b** s = 2.5 kPa; **c** s = 3.0 kPa; **d** s = 4.0 kPa, **e** evolution of large water clusters during the mini-trixial shearing test

distribution curves and be capable of contributing more strength on soil sample.

Later the proportion of the small clusters remains stable at s = 4.0 kPa upon axial strain as the specimen gets

almost drained during desaturation after applying suction (Fig. 14d). For the specimen under 4.0 kPa suction, except for the initial state, at each axis strain state during triaxial shearing has similar degree of saturation and there is little difference in strength comparing to the dry sample. The small-size water clusters inside the specimen are mainly the water film adsorbed on the surface of the soil particles, and the quantity of liquid bridges is insufficient. Therefore, the strength of the sample cannot be significantly enhanced.

In Fig. 14e, the evolution of large-volume water clusters during the mini-trixial shearing test is illustrated, in which it could be intuitively observed that the volume of large water clusters is decreasing with the development of axial strain. And the integrated variation tendency about the evolution of large-volume water clusters is corresponding to the decreased degree of saturation in Fig. 12c, which could be interpreted as the largest volume water cluster in sample occupying higher than 50% of total volume of liquid phase.

During the triaxial shearing process, the volume of the largest liquid clusters decreases correspondingly, and the quantity of small-volume liquid clusters in the liquid bridge increases. The main factor affecting the overall unsaturated strength of the sample is the small-volume liquid bridge and liquid cluster inside shear band.

### 4.3 Evolution of interfacial areas

In this paper, the interfacial area values are not only obtained from globally measuring for the whole specimens, but also measured locally based on the RVEs. The specific interfacial area is defined has the total air–water interfacial area divided by the total volume. The evolution of the global value of this specific interfacial area (for the full investigated domain) as a function of axial strain and degree of saturation is illustrated in Fig. 15a. It demonstrates a decreasing trend with the degree of saturation increase (induced by a lower maintained suction). And with the development of shear strain, the specific air–water interfacial area curve becomes lower, indicating that the air–water interfacial area is smaller when the sample density becomes lower even at the same degree of saturation. Meanwhile, Fig. 15b depicts the relationship between the ratio of wetted solid surface (solid–water interface normalised by the total solid phase surface, noted as $\chi_{sw}$) and degree of saturation. It shows that the ratio of wetted solid surface decreases as the degree of saturation decreases (a higher applied suction value) and the curve is generally higher than the $S_r = \chi_{sw}$ reference line. It can also be seen that the loading stage has little effect on the ratio of wetted solid surface.

Due to the heterogeneous phenomena of the porous media and the water phase, degree of saturation and the interfacial areas are various in different RVEs. Since the local RVEs cover the full range of degree of saturation and porosity, the local quantities may lead to a more comprehensive understanding. Figure 16 graphically expressed the relationship between the specific air–water interfacial area and the local degree of saturation for all RVEs. Comparing to the relatively monotonous trend between the two global parameters in Fig. 15a, it shows that the specific air–water interfacial area has a rising and then decline trend with degree of saturation increase. The peak value appears between 20 and 40% of saturation as there are more water meniscus in this range. Under each controlled suction condition, at the initial state ($\varepsilon = 0\%$), the degree of saturation of the sample is relatively high and there are more RVEs filled with water. And at the end state after shearing ($\varepsilon \approx 15\%$), the sample porosity is reduced and there are more water drains out from the RVEs leading the group of RVE data moving to the left.

The four graphs in Fig. 17 present the relationship between the ratio of wetted solid surface and the local degree of saturation for each RVE in samples. It can be seen that the wetted solid surface of each RVE is higher with the increase in local degree of saturation, but the relationship is not linear. The trend corresponds to the global curve in Fig. 15b. It is also observed that triaxial strain does not alter the distribution trend but only shift the data to the left. This means that after shearing there are more big pores influencing the global degree of saturation, however, the local ratio of wetted solid surface is mainly determined by the local degree of saturation.

During the triaxial shearing process, the distribution of the specific air–water interfacial area changes, but the distribution of the ratio of wetted solid-phase grains surface hardly changes but shifts. Nevertheless, when the unsaturated granular material undergoes triaxial shear, the contribution of the interface effect between phases to the unsaturated strength is not stable.

### 4.4 Evolution of coordination numbers

Figure 18 displays the evolution of mean coordination number (CN) of the sand samples during triaxial compression under four different suction conditions. In each suction controlled triaxial test, the mean coordination number of inter-particle contacts shows a decreasing trend with axial strain, which is corresponding to the increasing trend of sample void ratio during triaxial loading in Fig. 12b as a higher sample porosity leads to a lower coordination number. In the post-peak deviatoric stress stage (i.e. $\varepsilon \approx 10\%$–$15\%$), the mean coordination number of inter-particle contacts tends to be stabilized. For a higher applied suction (a lower degree of saturation), the final porosity is higher, and the mean coordination number is

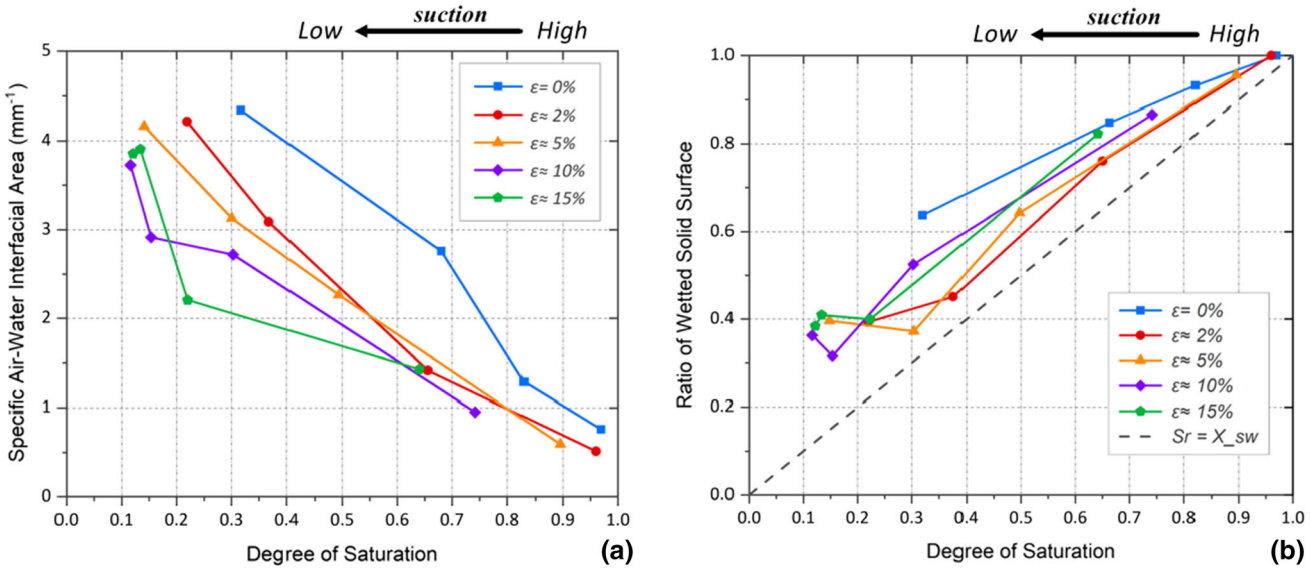


**Fig. 15** Global interfacial area evolution of the samples: **a** air–water interfacial area; **b** ratio of wetted solid surface area (solid–water interface divided by the total solid surface)

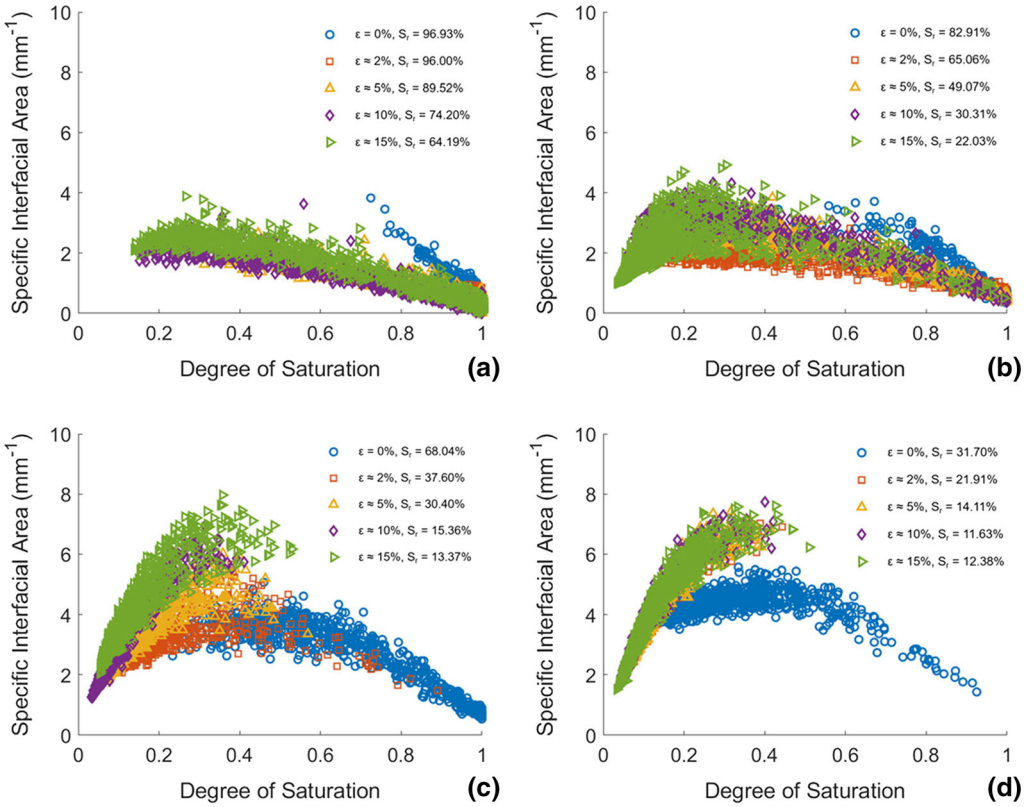


**Fig. 16** Air–water interfacial area analysis based on RVEs: **a** s = 2.0 kPa; **b** s = 2.5 kPa; **c** s = 3.0 kPa; **d** s = 4.0 kPa

correspondingly lower indicating that the microstructure is relatively looser.

The frequency distributions of coordination number (CN) of contacted soil particles at different axial strains under each suction condition are presented in Fig. 20. Each coordination number (CN) figure shows the similar trend that the peak of the curve shifts to the left with the increase in axial strain indicating that there are more particles losing their surrounding contacts. And the peak frequency of coordination number is higher when the mean coordination

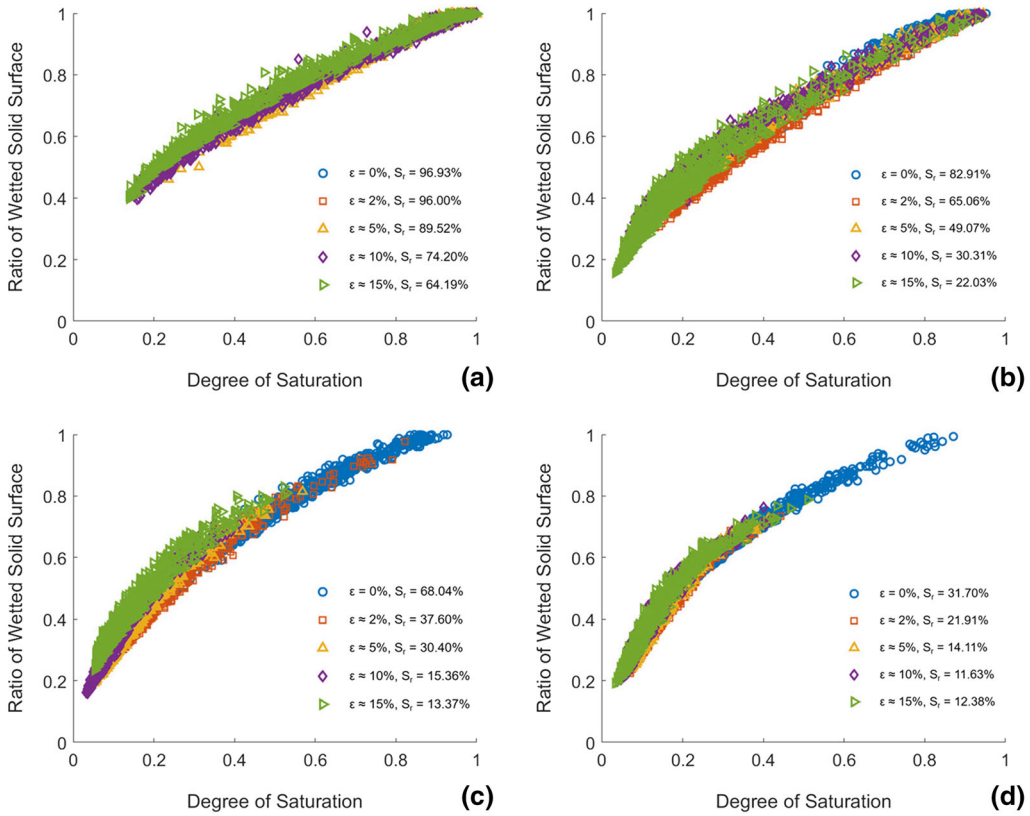


**Fig. 17** Wetted area (solid–water interface) analysis based on RVEs: **a** s = 2.0 kPa; **b** s = 2.5 kPa; **c** s = 3.0 kPa; **d** s = 4.0 kPa

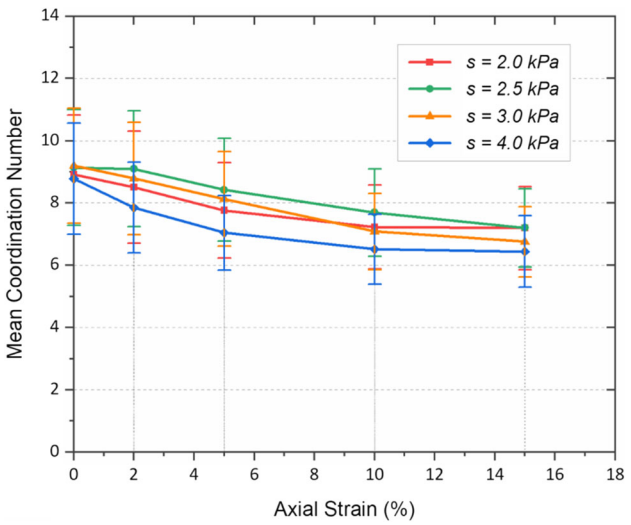


**Fig. 18** Evolution of mean coordination number during triaxial compression

number value corresponding to that curve is lower, which is consistent with the decrease trend of mean coordination number (CN) as the axial strain increase. As shown in Fig. 19, the peak value occurs at CN = 8 in the initial state, and the peak value moves to CN = 6 as the void ratio of the samples increases until the triaxial compression finished ($\varepsilon \approx 15\%$). Figure 20 compares the frequency distributions of coordination number (CN) of the soil samples at initial state ($\varepsilon = 0\%$) and after shearing ($\varepsilon \approx 15\%$) under different suction controlled conditions. In Fig. 20a, it shows that at the initial stage ($\varepsilon = 0\%$) suction value has little effect on the frequency distribution of coordination number. Figure 20b depicts the final stage distribution after triaxial shearing at $\varepsilon \approx 15\%$, and there is an evident growth in the peak frequency for all suction levels but the corresponding most frequent coordination numbers are all decreased. It can also be observed that at the final stage a higher suction level gives a higher peak frequency in coordination number. This is consistent with the observed higher dilatancy in triaxial compression when the maintained suction is increased.

## 4.5 Evolution of contact based fabric

Based on the analysis results (in Sect. 3.3) of the extracted inter-particle contacts, the spatial position information and normal vector of each inter-particle contact can be obtained to study the contact fabric evolution upon triaxial loading in unsaturated granular materials. According to the axial-symmetrical feature of the stress on the sample, the 3D distribution of the contact normal orientations can be

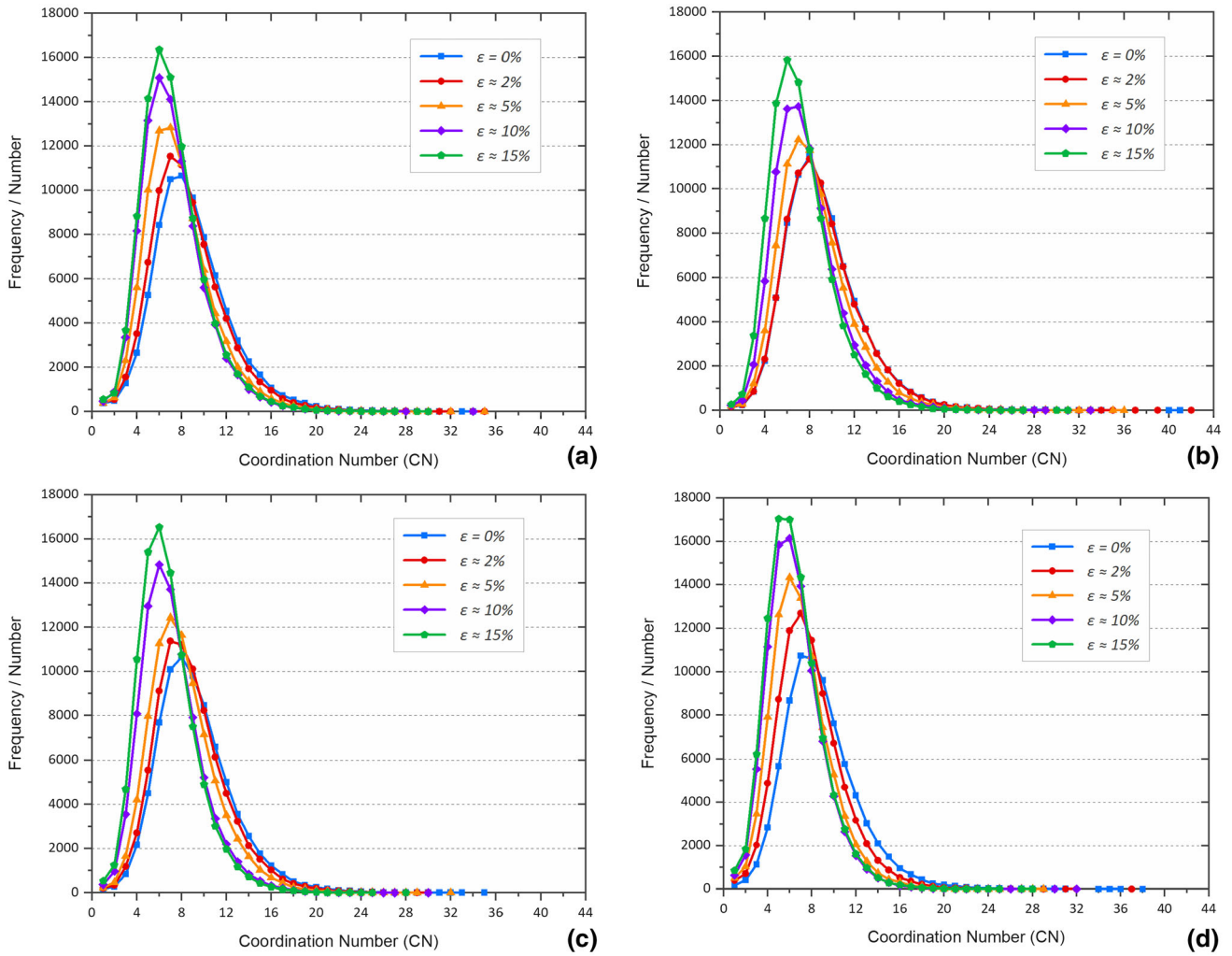


**Fig. 19** Probability density distributions of coordination number during triaxial compression: **a** s = 2.0 kPa; **b** s = 2.5 kPa; **c** s = 3.0 kPa; **d** s = 4.0 kPa

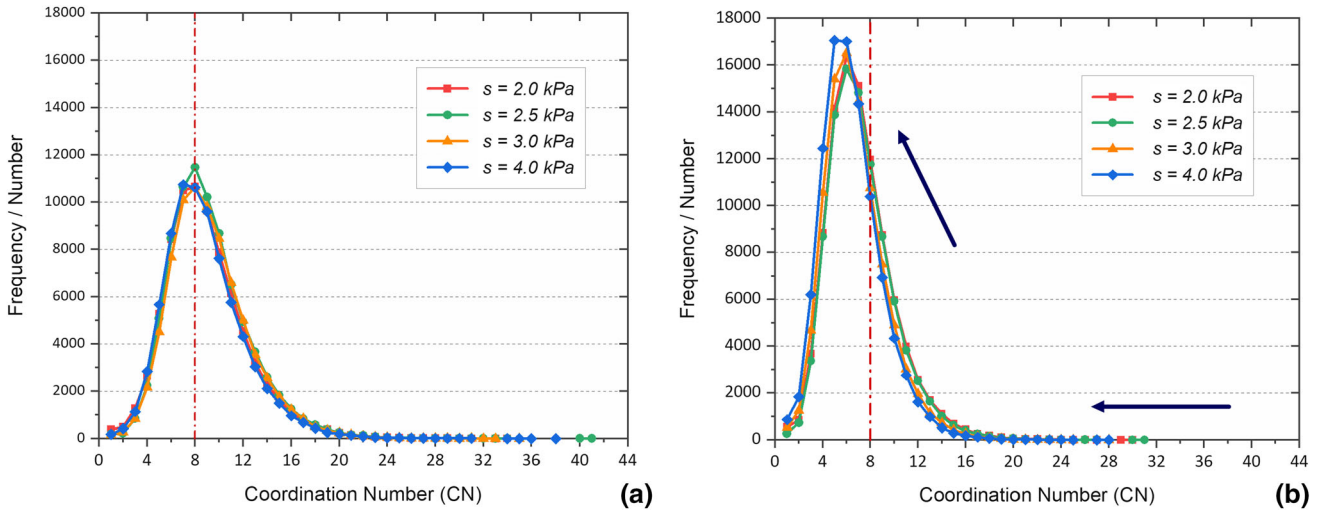


**Fig. 20** Probability density distributions of coordination number at initial state and after triaxial compression: **a** $\varepsilon_a = 0\%$; **b** $\varepsilon_a \approx 15\%$

converted to a 2D distribution. Each inter-particle contact has two contact normals, which are opposite of each other. Figure 21 illustrates all of the contact normals on a unit sphere. The $Z$ axis is the direction in which the axial strain is applied. The probability of a particular contact orientation with an angle $\varphi$ to the $z$ axis is estimated based on the circle band on the unit sphere with a tiny width of $\Delta\varphi$.

The probability of a particular direction is calculated as:

$$P(\varphi) = \frac{N_\varphi}{2\pi\left|\cos\left(\varphi - \frac{\Delta\varphi}{2}\right) - \cos\left(\varphi + \frac{\Delta\varphi}{2}\right)\right| N\Delta\varphi} \tag{3}$$

where $N_\varphi$ is the number of contact normals within the circle band and $N$ is the total number of contact normals (two times the total physical contact number). With this estimation method, the directional distribution of 3D angle data is converted to the $X$–$Z$ plane.

The directional distributions of contact normal of the sand specimens at different axial strain under 2.0 kPa, 2.5 kPa, 3.0 kPa and 4.0 kPa suction conditions are plotted in Fig. 22, which is used to analyse how the compressive stresses are transmitted in granular materials in triaxial shearing. The bin interval for the frequency calculation is 20°. It can be seen that the morphological and directional distributions of each group are similar; however, the probability of vertical contacts (along the $Z$ axis) decreases as the controlled suction of the samples increases. At the initial state of each group, the inter-particle contacts are not isotropically distributed, which reflects the contact anisotropies already existing in the sample due to gravity and the compaction process during sample preparation. For the samples with suction from 2.0 to 3.0 kPa, the probability of vertical contacts along the axial loading direction grows and the probability of horizontal contacts decreases as the axial strain increases, while their probabilities are basically identical at $\varepsilon \approx 10\%$ and $\varepsilon \approx 15\%$, which indicates that the fabric anisotropies of these samples evolve to a stable state.

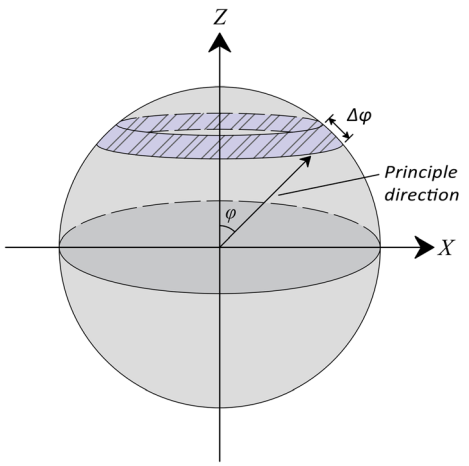


**Fig. 21** Principal directions on the unit sphere

Many fabric tensors have been proposed to characterize granular materials in terms of various directional data, such as contact normal vectors, particle orientations and void spaces. In order to express all orientations statistically, a fabric tensor is commonly used. The contact orientation moment tensor can be calculated by taking an average of the self-tensor product of the unit vector of the inter-particle contact normals [19]:

$$N_{ij} = \frac{1}{N_c}\sum_{c\in V} \mathbf{n}\otimes\mathbf{n} \tag{4}$$

where $N_c$ is the total number of inter-particle contacts and $\boldsymbol{n}$ is the unit vector of the contact orientation.

The anisotropy of a tensor is normally indicated by its deviatoric part. Then the deviatoric tensor of contact normals is calculated as:

$$D_{ij} = \frac{15}{2}\left(N_{ij} - \frac{1}{3}\delta_{ij}\right) \tag{5}$$

The anisotropy degree of contact fabric can be defined as the square root of the second tensor invariants of the above deviatoric tensor,

$$A = \sqrt{\left[(D_{11}-D_{22})^2+(D_{11}-D_{33})^2+(D_{22}-D_{33})^2\right]/2}.$$

Figure 23a shows the evolution of anisotropy degree $A$ of the four triaxial tests under different suction conditions. There is an obvious increase in fabric anisotropy upon triaxial shearing, and the anisotropy degree tends to be stable at large strain stages.

Under each suction condition, the contact orientation anisotropy at the initial state is almost concentrated nearly 0.15, except for the anisotropy of initial state under the 4 kpa suction condition (its anisotropy is slightly higher than 0.20). The anisotropy of the samples under each suction condition begins to increase rapidly as the triaxial shear progresses. And after the peak strength at $\varepsilon \approx 10\%$, the degree of anisotropy becomes stable or decreases slightly. For the phenomenon that the anisotropy of the samples is not close to 0 at the initial state, grain shape effect and compaction process under gravity may be considered as possible reasons. The tested Mol sand grains are basically in angular shape and the samples are prepared in a mold with compaction process before saturated, and this may lead to an obvious fabric anisotropy [39].

Figure 23b shows the change of anisotropy from its initial state in percentage. The suction effect on the ultimate change of anisotropy has a rise and fall trend as the sample with middle suction value (2.5 kPa) has the most significant anisotropy change while the sample with 4 kPa

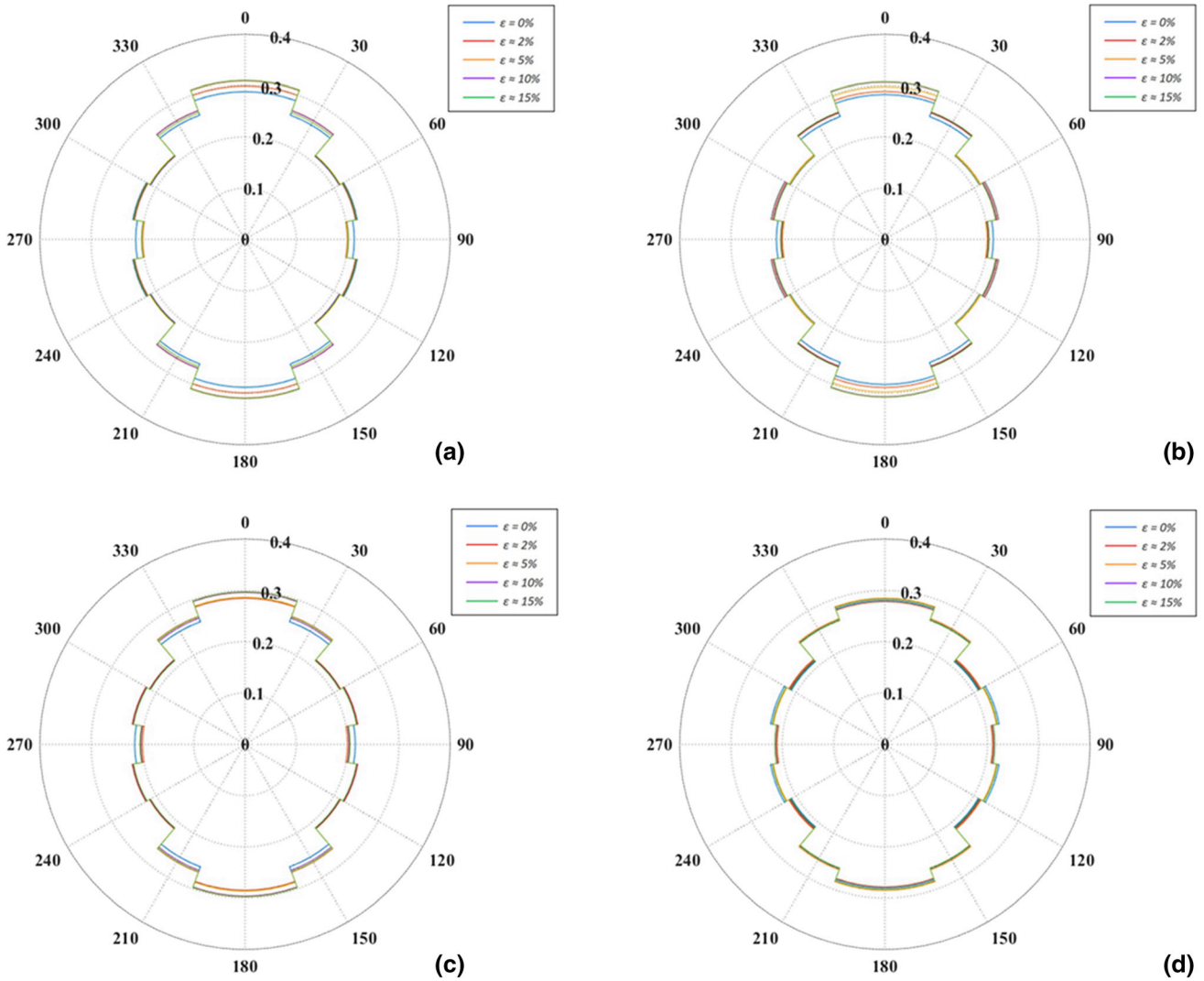


**Fig. 22** Directional distribution of contact orientations: **a** s = 2.0 kPa; **b** s = 2.5 kPa; **c** s = 3.0 kPa; **d** s = 4.0 kPa

has the lowest effect. The evolution of contact orientation anisotropy with axial strain basically resembles the axial strain–deviatoric stress curves (Fig. 12a). As for sandy soils, higher suction is not always increasing the material strength (it has small cohesion when it is nearly dried). And from the microscopic point of view, a stronger material can sustain a higher fabric anisotropy, that is why the sample with 2.5 kPa suction peaks the anisotropy value.

### 4.6 The anisotropic feature of suction induced stress

For unsaturated soil, the effective stress, initially proposed by Bishop, can be expressed as the net stress plus a stress term contributed by suction as:

$$\sigma_{ij}^{'} = \sigma_{ij} + u_a\delta_{ij} + \chi_{ij}(u_a - u_w) \tag{6}$$

where the Bishop's coefficient is recently regarded as a tensorial form of $\chi_{ij}$ by considering that the effect of suction may not be isotropic due to the anisotropic solid skeleton and the non-uniform water distribution.

Microscopically, for a small RVE, we may deduce the effective stress by subtracting the stress terms induced by pore air pressure $u_a$ acting on the non-wetted solid surface $S^{\mathrm{sa}}$, pore water pressure $u_w$ acting on the wetted surface $S^{\mathrm{sw}}$ and the interfacial forces $T_i$ acting on the solid–water–air triple lines $l^{\mathrm{swa}}$ from the total stress $\sigma_{ij}$:

$$\sigma_{ij}^{'} = \sigma_{ij} - \frac{3}{S}\int_{S^{\mathrm{sa}}} u_a n_i n_j \mathrm{d}S - \frac{3}{S}\int_{S^{\mathrm{sw}}} u_w n_i n_j \mathrm{d}S - \frac{3}{S}\int_{l^{\mathrm{swa}}} -T_i n_j \mathrm{d}l \tag{7}$$

where $S$ is the solid skeleton surface area and $n_i$ is the unit vector normal to the solid surface on the acting point. Then

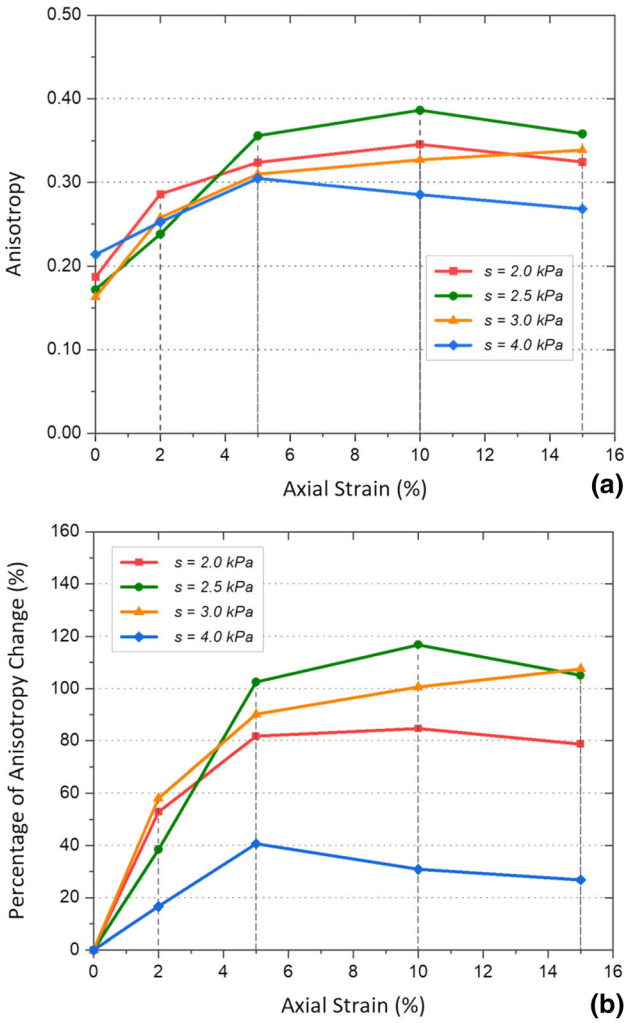


**Fig. 23** The anisotropic of contact orientation fabric: **a** evolution of contact orientation fabric anisotropy; **b** percentage of contact orientation fabric anisotropy change

it can be derived as the following format by taking $S\delta_{ij} = \int_{S^{sa}} n_i n_j \mathrm{d}S + \int_{S^{sw}} n_i n_j \mathrm{d}S$:

$$\sigma'_{ij} = \sigma_{ij} - u_a\delta_{ij} + \frac{3(u_a - u_w)}{S}\int_{S^{sw}} n_i n_j \mathrm{d}S + \frac{3}{S}\int_{l^{swa}} T_i n_j \mathrm{d}l \tag{8}$$

Combining with Eq. 6, the tensorial Bishop's coefficient can be written as:

$$\chi_{ij} = \frac{3}{S}\int_{S^{sw}} n_i n_j \mathrm{d}S + \frac{3}{S(u_a - u_w)}\int_{l^{swa}} T_i n_j \mathrm{d}l \tag{9}$$

in which the first term is related to the wetted solid surface and the second term is related to interfacial surface tension force as well as the suction level. Due to the limitation of image resolution (9 μm/pixel in this study), it is still not easy to detect the directions of the interface on the solid surface. Furthermore, it can be easily deduced that the anisotropy of the second term is related to the wetted surface (the first term). In this study, we mainly discuss the anisotropic nature of the water phase based on the CT image evidence; therefore, only the first term (the wetted area) is considered to measure $\chi_{ij}$. Based on the CT images, the tensorial form of Bishop's coefficient can be simplified as:

$$\chi_{ij} \approx \begin{bmatrix} \frac{3S_{11}^{sw}}{S} & & \\ & \frac{3S_{22}^{sw}}{S} & \\ & & \frac{3S_{33}^{sw}}{S} \end{bmatrix} \tag{10}$$

where $S_{11}^{sw}$, $S_{22}^{sw}$ and $S_{33}^{sw}$ are wetted solid phase pixels normal to the three principle directions, respectively, and $S$ is the total surface pixels of the solid phase in the three-dimensional CT images. Similar to anisotropy degree of solid contacts, the anisotropy in suction and the 'Bishop's coefficient' can be defined from the deviatoric part of $\chi_{ij}$ as follows:

$$A_w = \sqrt{3J_2\left(\frac{\chi_{ij}}{\chi_{ii}} - \frac{1}{3}\delta_{ij}\right)} = \sqrt{\frac{3}{2}}\left\|\frac{\chi_{ij}}{\chi_{ii}} - \frac{1}{3}\delta_{ij}\right\| \tag{11}$$

Figure 24 depicts the evolution of the Bishop's coefficients calculated from the CT images in the three principle directions of the four tested samples. It can be seen that although the $\chi$ values in the three principle directions are similar before triaxial test, the discrepancies of $\chi$ between the first principle direction and the two other principle directions are enlarged upon triaxial loading. The $\chi$ values in the middle and minor principle directions, in which the confining pressures are maintained, are always the same. Figure 25 presents the evolutions of the mean and the degree of anisotropy of the tensorial form of Bishop's coefficient, which are estimated from the three dimensional CT images. In Fig. 25a, the mean value of Bishop's coefficient, which is associated to the percentage of wetted solid surface area, is reduced by higher suction. It can also be seen that the mean $\chi$ value is also reduced by triaxial shearing which is coincide with the decline trend of degree of saturation in Fig. 12c. In Fig. 25b, the evolution of degree of anisotropy in $\chi_{ij}$ is depicted. It can be seen that with the decrease in degree of saturation (increase in suction) the initial anisotropy effect of suction is increase. And with the development of triaxial strain, the effect of anisotropy in suction becomes even more significant, which is induced by the liquid phase migration during the triaxial deformation. The trend also indicates that with a lower degree of saturation the water phase is more likely to present as an anisotropic effect.

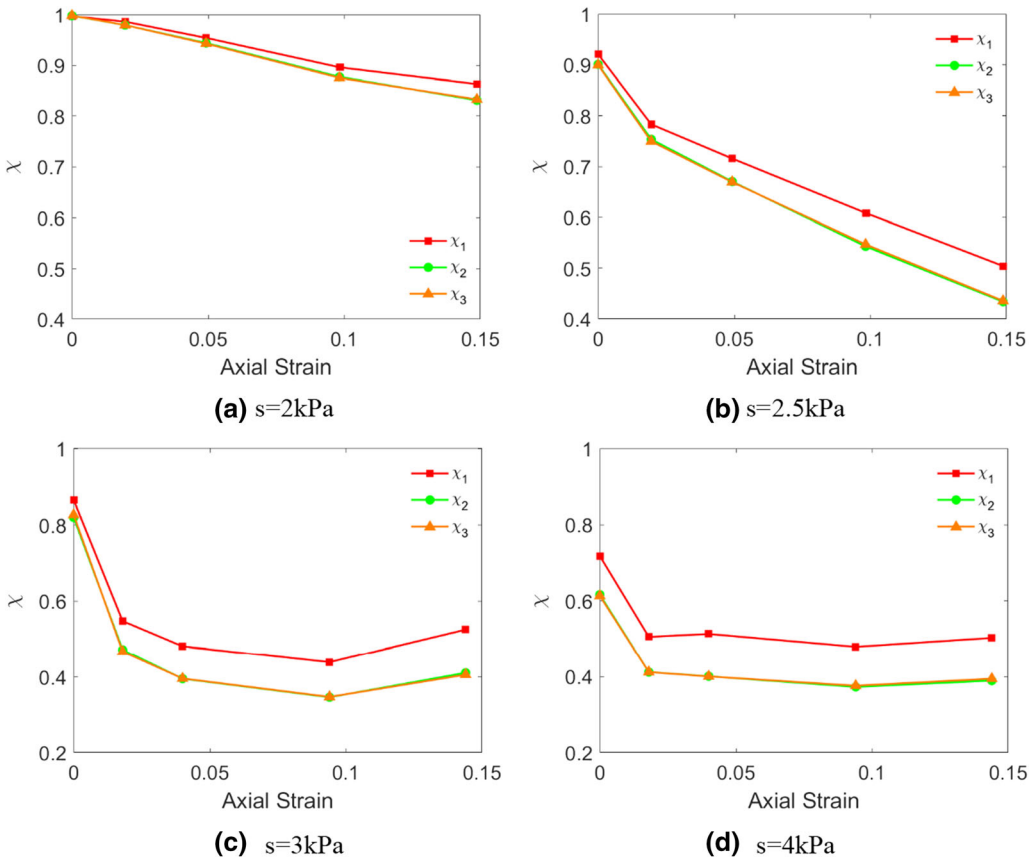


**Fig. 24** Bishop's coefficient in three principle directions: **a** s = 2 kPa **b** s = 2.5 kPa **c** s = 3 kPa **d** s = 4 kPa

## 5 Concluding remarks

A self-designed suction-controlled mini-triaxial device is developed in which the sample size is miniaturized and the cell is made of transparent Plexiglas. With this device, unsaturated sands can be tested under different suction levels while X-ray CT scanned images are implemented at different loading stages. The obtained image resolution is down to 9 μm/pixel under the scan of a 100 kV X-ray source under 10 W power. After image 3D reconstruction, image trinarization, label analysis, contact detection, and other customized image analysis and calculation, the micro-mechanisms of unsaturated granular soils upon triaxial shearing can be investigated.

The unsaturated fine sand shows a dilation behaviour during triaxial shearing. In unsaturated samples, the strength and dilatancy are higher than those of the dry material. It is also observed that the material strength is not monotonically increased by suction increase which means there is an optimal suction/degree of saturation (s = 2.5 kPa in this case).

During the triaxial loading, as the solid structure becomes looser, the observed inter-particle contact coordination number is also in a decline trend until a steady state at large strain states. The sample with s = 2.5 kPa, which has the highest strength, also has the highest coordination number. Fabric anisotropy of the solid structures can also be quantified based on the inter-particle contact normal. Due to the gravity effect and the compaction procedures in sample preparation, there is a significant initial fabric anisotropy in all samples and the triaxial loading, however, enlarged the anisotropy. The sample with s = 2.5 kPa, in which the capillarity effect is the strongest, has the largest loading induced fabric anisotropy.

Water drains out after triaxial shear if suction is maintained. As the shear band develops, the volume of the largest liquid clusters decreases correspondingly, and the quantity of small-volume liquid clusters in the liquid bridge increases. Triaxial loading also shifts the distributions of inter-facial areas. The maximum air–water interfacial area appears in 20% to 40% degree of saturation and a higher suction level also gives more interfaces.

The effective stress definition can be re-interpreted microscopically based on small RVEs. Associated to the anisotropic solid structure and the heterogeneity nature of the water phase, the suction-induced stress component is not an isotropic term. The tensorial form of Bishop's coefficient can be roughly estimated from the CT images

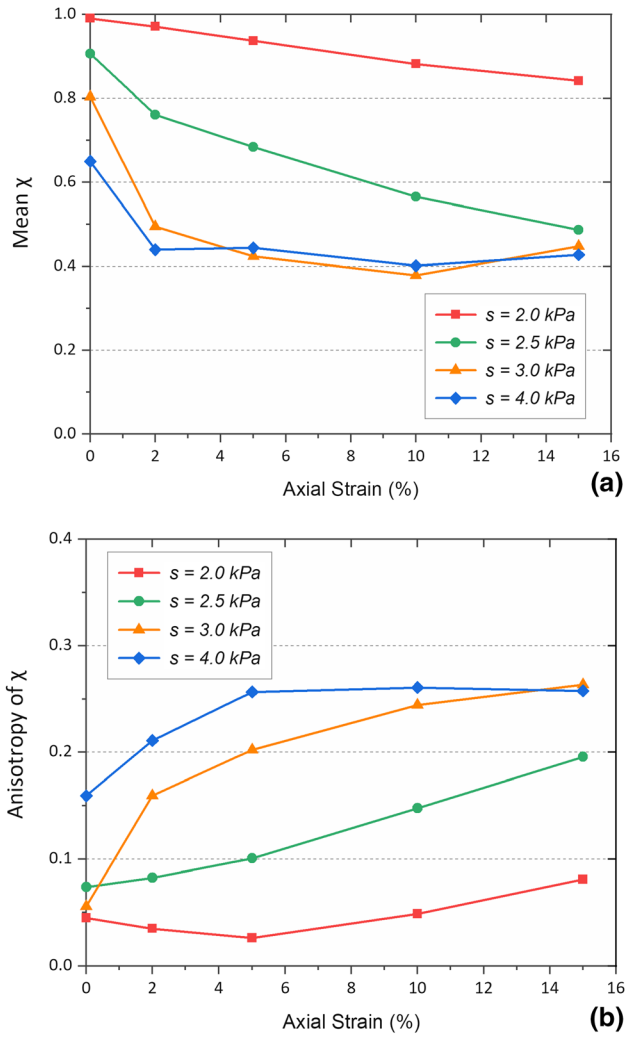


**Fig. 25** The anisotropic feature of suction induced stress: **a** mean Bishop's coefficient **b** anisotropy of suction induced stress

and the anisotropic effect is proved. The degree of anisotropy in the suction stress term is increased with triaxial loading and the anisotropy of the water phase is more obvious in samples with a lower degree of saturation in which there are more isolated water bridges around solid contacts.

**Acknowledgements** This work was funded by F.R.S-FNRS of Belgium (PDR.T.1002.14) and NFSC of China (Nos: 51909139, 52011530458). The first author also acknowledges the support of Taishan Scholar Project of Shandong Province of China.

**Data availability** All data are available upon reasonable request from the corresponding author.

## References

1. Alonso EE, Pereira J-M, Vaunat J, Olivella S (2010) A microstructurally based effective stress for unsaturated soils. Géotechnique 60:913–925. https://doi.org/10.1680/geot.8.P.002
2. Andò E, Hall SA, Viggiani G, Desrues J, Bésuelle P (2012) Grain-scale experimental investigation of localised deformation in sand: a discrete particle tracking approach. Acta Geotech 7:1–13. https://doi.org/10.1007/s11440-011-0151-6
3. Andò E, Hall SA, Viggiani G, Desrues J, Bésuelle P (2012) Experimental micromechanics: grain-scale observation of sand deformation. Géotech Lett 2:107–112. https://doi.org/10.1680/geolett.12.00027
4. Bruchon J-F, Pereira J-M, Vandamme M, Lenoir N, Delage P, Bornert M (2013) Full 3D investigation and characterisation of capillary collapse of a loose unsaturated sand using X-ray CT. Granul Matter 15:783–800. https://doi.org/10.1007/s10035-013-0452-6
5. Cheng Z, Zhou B, Wang J (2020) Tracking particles in sands based on particle shape parameters. Adv Powder Technol 31:2005–2019. https://doi.org/10.1016/j.apt.2020.02.033
6. Cnudde V, Boone MN (2013) High-resolution X-ray computed tomography in geosciences: a review of the current technology and applications. Earth-Sci Rev 123:1–17. https://doi.org/10.1016/j.earscirev.2013.04.003
7. Cnudde V, Cwirzen A, Masschaele B, Jacobs PJS (2009) Porosity and microstructure characterization of building stones and concretes. Eng Geol 103:76–83. https://doi.org/10.1016/J.ENGGEO.2008.06.014
8. Cormack AM (1973) Reconstruction of densities from their projections, with applications in radiological physics. Phys Med Biol 18:195–207. https://doi.org/10.1088/0031-9155/18/2/003
9. Dalla E, Hilpert M, Miller CT (2002) Computation of the interfacial area for two-fluid porous medium systems. J Contam Hydrol 56:25–48. https://doi.org/10.1016/S0169-7722(01)00202-9
10. Desrues J, Chambon R, Mokni M, Mazerolle F (1996) Void ratio evolution inside shear bands in triaxial sand specimens studied by computed tomography. Géotechnique 46:529–546. https://doi.org/10.1680/geot.1996.46.3.529
11. Duriez J, Wan R (2017) Contact angle mechanical influence in wet granular soils. Acta Geotech 12:67–83. https://doi.org/10.1007/s11440-016-0500-6
12. Duriez J, Wan R, Pouragha M, Darve F (2018) Revisiting the existence of an effective stress for wet granular soils with micromechanics. Int J Numer Anal Methods Geomech 42:959–978. https://doi.org/10.1002/nag.2774
13. Hall SA, Bornert M, Desrues J, Pannier Y, Lenoir N, Viggiani G, Bésuelle P (2010) Discrete and continuum analysis of localised deformation in sand using X-ray μCT and volumetric digital image correlation. Géotechnique 60:315–322. https://doi.org/10.1680/geot.2010.60.5.315
14. Higo Y, Oka F, Kimoto S, Sanagawa T, Matsushima Y (2011) Study of strain localization and microstructural changes in partially saturated sand during triaxial tests using microfocus X-ray CT. Soils Found 51:95–111. https://doi.org/10.3208/sandf.51.95
15. Higo Y, Oka F, Sato T, Matsushima Y, Kimoto S (2013) Investigation of localized deformation in partially saturated sand under triaxial compression using microfocus X-ray CT with digital image correlation. Soils Found 53:181–198. https://doi.org/10.1016/j.sandf.2013.02.001
16. Hou X, Vanapalli SK, Li T (2019) Wetting-induced collapse behavior associated with infiltration: a case study. Eng Geol 258:105146. https://doi.org/10.1016/J.ENGGEO.2019.105146

17. Hounsfield GN (1973) Computerized transverse axial scanning (tomography): part 1 description of system. Br J Radiol 46:1016–1022. https://doi.org/10.1259/0007-1285-46-552-1016
18. Wang JP, Lambert P, Kock T, Cnudde V, François B (2019) Investigation of the effect of specific interfacial area on strength of unsaturated granular materials by X-ray tomography. Acta Geotech 14:1545–1559. https://doi.org/10.1007/s11440-019-00765-2
19. Kanatani K-I (1984) Distribution of directional data and fabric tensors. Int J Eng Sci 22:149–164
20. Ketcham RA, Carlson WD (2001) Acquisition, optimization and interpretation of X-ray computed tomographic imagery: applications to the geosciences. Comput Geosci 27:381–400. https://doi.org/10.1016/S0098-3004(00)00116-3
21. Khaddour G, Riedel I, Andò E, Charrier P, Bésuelle P, Desrues J, Viggiani G, Salager S (2018) Grain-scale characterization of water retention behaviour of sand using X-ray CT. Acta Geotech 13:497–512. https://doi.org/10.1007/s11440-018-0628-7
22. Kido R, Higo Y (2020) Microscopic characteristics of partially saturated dense sand and their link to macroscopic responses under triaxial compression conditions. Acta Geotech 15:3055–3073. https://doi.org/10.1007/s11440-020-01049-w
23. Kido R, Higo Y, Takamura F, Morishita R, Khaddour G, Salager S (2020) Morphological transitions for pore water and pore air during drying and wetting processes in partially saturated sand. Acta Geotech 15:1745–1761. https://doi.org/10.1007/s11440-020-00939-3
24. Koliji A, Vulliet L, Laloui L (2010) Structural characterization of unsaturated aggregated soil. Can Geotech J 47:297–311. https://doi.org/10.1139/T09-089
25. Laloui L, Nuth M (2009) On the use of the generalised effective stress in the constitutive modelling of unsaturated soils. Comput Geotech 36:20–23. https://doi.org/10.1016/j.compgeo.2008.03.002
26. Lu N, Godt JW, Wu DT (2010) A closed-form equation for effective stress in unsaturated soil. Water Resour Res 46:W05515. https://doi.org/10.1029/2009WR008646
27. Manahiloh K, Muhunthan B (2012) Characterizing liquid phase fabric of unsaturated specimens from X-ray computed tomography images. In: Mancuso C, Jommi C, D'Onza F (eds) Unsaturated soils: research and applications. Springer, Berlin Heidelberg, pp 71–80
28. Milatz M, Hüsener N, Andò E, Viggiani G, Grabe J (2021) Quantitative 3D imaging of partially saturated granular materials under uniaxial compression. Acta Geotech 2021:1–28. https://doi.org/10.1007/S11440-021-01315-5
29. Moscariello M, Cuomo S, Salager S (2017) Capillary collapse of loose pyroclastic unsaturated sands characterized at grain scale. Acta Geotech. https://doi.org/10.1007/s11440-017-0603-8
30. Pan C, Hilpert M, Miller CT (2004) Lattice-Boltzmann simulation of two-phase flow in porous media. Water Resour Res. https://doi.org/10.1029/2003WR002120
31. Richefeu V, Radjai F, Delenne J-Y (2016) Lattice Boltzmann modelling of liquid distribution in unsaturated granular media. Comput Geotech 80:353–359. https://doi.org/10.1016/j.compgeo.2016.02.017
32. Riedel I, Andò E, Salager S, Bésuelle P, Viggiani G (2012) Water retention behaviour explored by X-ray CT analysis. Unsaturated soils: research and applications. Springer Berlin Heidelberg, Berlin, Heidelberg, pp 81–88
33. Scheel M, Seemann R, Brinkmann M, Di Michiel M, Sheppard A, Breidenbach B, Herminghaus S (2008) Morphological clues to wet granular pile stability. Nat Mater 7:189–193. https://doi.org/10.1038/nmat2117
34. Scholtès L, Chareyre B, Nicot F, Darve F (2009) Micromechanics of granular materials with capillary effects. Int J Eng Sci 47:64–75. https://doi.org/10.1016/j.ijengsci.2008.07.002
35. Sleutel S, Cnudde V, Masschaele B, Vlassenbroek J, Dierick M, Van Hoorebeke L, Jacobs P, De Neve S (2008) Comparison of different nano- and micro-focus X-ray computed tomography set-ups for the visualization of the soil microstructure and soil organic matter. Comput Geosci 34:931–938. https://doi.org/10.1016/j.cageo.2007.10.006
36. Smethurst J, Clarke D, Powrie W (2012) Factors controlling the seasonal variation in soil water content and pore water pressures within a lightly vegetated clay slope. Géotechnique 62:429–446
37. Sonon B, François B, Massart TJ (2012) A unified level set based methodology for fast generation of complex microstructural multi-phase RVEs. Comput Methods Appl Mech Eng 223–224:103–122. https://doi.org/10.1016/j.cma.2012.02.018
38. Taina IA, Heck RJ, Elliot TR (2008) Application of X-ray computed tomography to soil science: a literature review. Can J Soil Sci 88:1–19. https://doi.org/10.4141/CJSS06027
39. Vijayan A, Annabattula RK (2019) Effect of particle flow dynamics on the fabric evolution in spherical granular assemblies filled under gravity. Powder Technol 356:909–919. https://doi.org/10.1016/J.POWTEC.2019.09.027
40. Vlahinić I, Andò E, Viggiani G, Andrade J (2014) Towards a more accurate characterization of granular media: extracting quantitative descriptors from tomographic images. Granul Matter 16:9–21. https://doi.org/10.1007/s10035-013-0460-6
41. Wang J-P, Andò E, Charrier P, Salager S, Lambert P, François B (2019) Micro-scale investigation of unsaturated sand in mini-triaxial shearing using X-ray CT. Géotechnique Lett 9:269–277. https://doi.org/10.1680/jgele.18.00214
42. Wang J-P, Li X, Yu H-S (2018) A micro–macro investigation of the capillary strengthening effect in wet granular materials. Acta Geotech 13:513–533. https://doi.org/10.1007/s11440-017-0619-0
43. Wang JP, Li X, Yu HS (2017) Stress-force-fabric relationship for unsaturated granular materials in pendular states. J Eng Mech 143:1–18. https://doi.org/10.1061/(ASCE)EM.1943-7889.0001283
44. Wang JP, Zeng GH, Yu HS (2019) A DEM investigation of water-bridged granular materials at the critical state. Comput Part Mech 6:637–655. https://doi.org/10.1007/s40571-019-00243-2
45. Wildenschild D, Sheppard AP (2013) X-ray imaging and analysis techniques for quantifying pore-scale structure and processes in subsurface porous medium systems. Adv Water Resour 51:217–246. https://doi.org/10.1016/j.advwatres.2012.07.018
46. Xu F, Liang S, Zhang Y, Li B, Hu Y (2021) Numerical study of water–air distribution in unsaturated soil by using lattice Boltzmann method. Comput Math with Appl 81:573–587. https://doi.org/10.1016/j.camwa.2019.08.013